# Measurement of inclusive charged-particle jet production in Au + Au collisions at $\sqrt{s_{NN}} = 200$ GeV

J. Adam,[6] L. Adamczyk,[2] J. R. Adams,[39] J. K. Adkins,[30] G. Agakishiev,[28] M. M. Aggarwal,[41] Z. Ahammed,[61] I. Alekseev,[3,35]
D. M. Anderson,[55] A. Aparin,[28] E. C. Aschenauer,[6] M. U. Ashraf,[11] F. G. Atetalla,[29] A. Attri,[41] G. S. Averichev,[28]
V. Bairathi,[53] K. Barish,[10] A. Behera,[52] R. Bellwied,[20] A. Bhasin,[27] J. Bielcik,[14] J. Bielcikova,[38] L. C. Bland,[6]
I. G. Bordyuzhin,[3] J. D. Brandenburg,[49,6] A. V. Brandin,[35] J. Butterworth,[45] H. Caines,[64] M. Calderón de la Barca Sánchez,[8]
D. Cebra,[8] I. Chakaberia,[29,6] P. Chaloupka,[14] B. K. Chan,[9] F-H. Chang,[37] Z. Chang,[6] N. Chankova-Bunzarova,[28]
A. Chatterjee,[11] D. Chen,[10] J. H. Chen,[18] X. Chen,[48] Z. Chen,[49] J. Cheng,[57] M. Cherney,[13] M. Chevalier,[10] S. Choudhury,[18]
W. Christie,[6] X. Chu,[6] H. J. Crawford,[7] M. Csanád,[16] M. Daugherity,[1] T. G. Dedovich,[28] I. M. Deppner,[19]
A. A. Derevschikov,[43] L. Didenko,[6] X. Dong,[31] J. L. Drachenberg,[1] J. C. Dunlop,[6] T. Edmonds,[44] N. Elsey,[63] J. Engelage,[7]
G. Eppley,[45] R. Esha,[52] S. Esumi,[58] O. Evdokimov,[12] A. Ewigleben,[32] O. Eyser,[6] R. Fatemi,[30] S. Fazio,[6] P. Federic,[38]
J. Fedorisin,[28] C. J. Feng,[37] Y. Feng,[44] P. Filip,[28] E. Finch,[51] Y. Fisyak,[6] A. Francisco,[64] L. Fulek,[2] C. A. Gagliardi,[55]
T. Galatyuk,[15] F. Geurts,[45] A. Gibson,[60] K. Gopal,[23] D. Grosnick,[60] W. Guryn,[6] A. I. Hamad,[29] A. Hamed,[5] S. Harabasz,[15]
J. W. Harris,[64] S. He,[11] W. He,[18] X. He,[26] S. Heppelmann,[8] S. Heppelmann,[42] N. Herrmann,[19] E. Hoffman,[20] L. Holub,[14]
Y. Hong,[31] S. Horvat,[64] Y. Hu,[18] H. Z. Huang,[9] S. L. Huang,[52] T. Huang,[37] X. Huang,[57] T. J. Humanic,[39] P. Huo,[52] G. Igo,[9]
D. Isenhower,[1] P. M. Jacobs,[31] W. W. Jacobs,[25] C. Jena,[23] A. Jentsch,[6] Y. JI,[48] J. Jia,[6,52] K. Jiang,[48] S. Jowzaee,[63] X. Ju,[48]
E. G. Judd,[7] S. Kabana,[53] M. L. Kabir,[10] S. Kagamaster,[32] D. Kalinkin,[25] K. Kang,[57] D. Kapukchyan,[10] K. Kauder,[6] H. W. Ke,[6]
D. Keane,[29] A. Kechechyan,[28] M. Kelsey,[31] Y. V. Khyzhniak,[35] D. P. Kikoła,[62] C. Kim,[10] B. Kimelman,[8] D. Kincses,[16]
T. A. Kinghorn,[8] I. Kisel,[17] A. Kiselev,[6] A. Kisiel,[62] M. Kocan,[14] L. Kochenda,[35] L. K. Kosarzewski,[14] L. Kramarik,[14]
P. Kravtsov,[35] K. Krueger,[4] N. Kulathunga Mudiyanselage,[20] L. Kumar,[41] R. Kunnawalkam Elayavalli,[63] J. H. Kwasizur,[25]
R. Lacey,[52] S. Lan,[11] J. M. Landgraf,[6] J. Lauret,[6] A. Lebedev,[6] R. Lednicky,[28] J. H. Lee,[6] Y. H. Leung,[31] C. Li,[48] W. Li,[50]
W. Li,[45] X. Li,[48] Y. Li,[57] Y. Liang,[29] R. Licenik,[38] T. Lin,[55] Y. Lin,[11] M. A. Lisa,[39] F. Liu,[11] H. Liu,[25] P. Liu,[52] P. Liu,[50]
T. Liu,[64] X. Liu,[39] Y. Liu,[55] Z. Liu,[48] T. Ljubicic,[6] W. J. Llope,[63] R. S. Longacre,[6] N. S. Lukow,[54] S. Luo,[12] X. Luo,[11]
G. L. Ma,[50] L. Ma,[18] R. Ma,[6] Y. G. Ma,[50] N. Magdy,[12] R. Majka,[64] D. Mallick,[36] S. Margetis,[29] C. Markert,[56] H. S. Matis,[31]
J. A. Mazer,[46] N. G. Minaev,[43] S. Mioduszewski,[55] B. Mohanty,[36] M. M. Mondal,[52] I. Mooney,[63] Z. Moravcova,[14]
D. A. Morozov,[43] M. Nagy,[16] J. D. Nam,[54] Md. Nasim,[22] K. Nayak,[11] D. Neff,[9] J. M. Nelson,[7] D. B. Nemes,[64] M. Nie,[49]
G. Nigmatkulov,[35] T. Niida,[58] L. V. Nogach,[43] T. Nonaka,[58] G. Odyniec,[31] A. Ogawa,[6] S. Oh,[31] V. A. Okorokov,[35] B. S. Page,[6]
R. Pak,[6] A. Pandav,[36] Y. Panebratsev,[28] B. Pawlik,[40] D. Pawlowska,[62] H. Pei,[11] C. Perkins,[7] L. Pinsky,[20] R. L. Pintér,[16]
J. Pluta,[62] J. Porter,[31] M. Posik,[54] N. K. Pruthi,[41] M. Przybycien,[2] J. Putschke,[63] H. Qiu,[26] A. Quintero,[54]
S. K. Radhakrishnan,[29] S. Ramachandran,[30] R. L. Ray,[56] R. Reed,[32] H. G. Ritter,[31] J. B. Roberts,[45] O. V. Rogachevskiy,[28]
J. L. Romero,[8] L. Ruan,[6] J. Rusnak,[38] N. R. Sahoo,[49] H. Sako,[58] S. Salur,[46] J. Sandweiss,[64] S. Sato,[58] W. B. Schmidke,[6]
N. Schmitz,[33] B. R. Schweid,[52] F. Seck,[15] J. Seger,[13] M. Sergeeva,[9] R. Seto,[10] P. Seyboth,[33] N. Shah,[24] E. Shahaliev,[28]
P. V. Shanmuganathan,[6] M. Shao,[48] F. Shen,[49] W. Q. Shen,[50] S. S. Shi,[11] Q. Y. Shou,[50] E. P. Sichtermann,[31] R. Sikora,[2]
M. Simko,[38] J. Singh,[41] S. Singha,[26] N. Smirnov,[64] W. Solyst,[25] P. Sorensen,[6] H. M. Spinka,[4] B. Srivastava,[44]
T. D. S. Stanislaus,[60] M. Stefaniak,[62] D. J. Stewart,[64] M. Strikhanov,[35] B. Stringfellow,[44] A. A. P. Suaide,[47] M. Sumbera,[38]
B. Summa,[42] X. M. Sun,[11] X. Sun,[12] Y. Sun,[48] Y. Sun,[21] B. Surrow,[54] D. N. Svirida,[3] P. Szymanski,[62] A. H. Tang,[6] Z. Tang,[48]
A. Taranenko,[35] T. Tarnowsky,[34] J. H. Thomas,[31] A. R. Timmins,[20] D. Tlusty,[13] M. Tokarev,[28] C. A. Tomkiel,[32]
S. Trentalange,[9] R. E. Tribble,[55] P. Tribedy,[6] S. K. Tripathy,[16] O. D. Tsai,[9] Z. Tu,[6] T. Ullrich,[6] D. G. Underwood,[4] I. Upsal,[49,6]
G. Van Buren,[6] J. Vanek,[38] A. N. Vasiliev,[43] I. Vassiliev,[17] F. Videbæk,[6] S. Vokal,[28] S. A. Voloshin,[63] F. Wang,[44] G. Wang,[9]
J. S. Wang,[21] P. Wang,[48] Y. Wang,[11] Y. Wang,[57] Z. Wang,[49] J. C. Webb,[6] P. C. Weidenkaff,[19] L. Wen,[9] G. D. Westfall,[34]
H. Wieman,[31] S. W. Wissink,[25] R. Witt,[59] Y. Wu,[10] Z. G. Xiao,[57] G. Xie,[31] W. Xie,[44] H. Xu,[21] N. Xu,[31] Q. H. Xu,[49] Y. F. Xu,[50]
Y. Xu,[49] Z. Xu,[6] Z. Xu,[9] C. Yang,[49] Q. Yang,[49] S. Yang,[6] Y. Yang,[37] Z. Yang,[11] Z. Ye,[45] Z. Ye,[12] L. Yi,[49] K. Yip,[6]
H. Zbroszczyk,[62] W. Zha,[48] D. Zhang,[11] S. Zhang,[48] S. Zhang,[50] X. P. Zhang,[57] Y. Zhang,[48] Y. Zhang,[11] Z. J. Zhang,[37]
Z. Zhang,[6] Z. Zhang,[12] J. Zhao,[44] C. Zhong,[50] C. Zhou,[50] X. Zhu,[57] Z. Zhu,[49] M. Zurek,[31] and M. Zyzak[17]

(STAR Collaboration)

[1]*Abilene Christian University, Abilene, Texas 79699*
[2]*AGH University of Science and Technology, FPACS, Cracow 30-059, Poland*
[3]*Alikhanov Institute for Theoretical and Experimental Physics NRC "Kurchatov Institute," Moscow 117218, Russia*
[4]*Argonne National Laboratory, Argonne, Illinois 60439*
[5]*American University of Cairo, New Cairo 11835, New Cairo, Egypt*
[6]*Brookhaven National Laboratory, Upton, New York 11973*
[7]*University of California, Berkeley, California 94720*

[8]*University of California, Davis, California 95616*
[9]*University of California, Los Angeles, California 90095*
[10]*University of California, Riverside, California 92521*
[11]*Central China Normal University, Wuhan, Hubei 430079*
[12]*University of Illinois at Chicago, Chicago, Illinois 60607*
[13]*Creighton University, Omaha, Nebraska 68178*
[14]*Czech Technical University in Prague, FNSPE, Prague 115 19, Czech Republic*
[15]*Technische Universität Darmstadt, Darmstadt 64289, Germany*
[16]*ELTE Eötvös Loránd University, Budapest, Hungary H-1117*
[17]*Frankfurt Institute for Advanced Studies FIAS, Frankfurt 60438, Germany*
[18]*Fudan University, Shanghai, 200433*
[19]*University of Heidelberg, Heidelberg 69120, Germany*
[20]*University of Houston, Houston, Texas 77204*
[21]*Huzhou University, Huzhou, Zhejiang 313000*
[22]*Indian Institute of Science Education and Research (IISER), Berhampur 760010, India*
[23]*Indian Institute of Science Education and Research (IISER) Tirupati, Tirupati 517507, India*
[24]*Indian Institute Technology, Patna, Bihar 801106, India*
[25]*Indiana University, Bloomington, Indiana 47408*
[26]*Institute of Modern Physics, Chinese Academy of Sciences, Lanzhou, Gansu 730000*
[27]*University of Jammu, Jammu 180001, India*
[28]*Joint Institute for Nuclear Research, Dubna 141 980, Russia*
[29]*Kent State University, Kent, Ohio 44242*
[30]*University of Kentucky, Lexington, Kentucky 40506-0055*
[31]*Lawrence Berkeley National Laboratory, Berkeley, California 94720*
[32]*Lehigh University, Bethlehem, Pennsylvania 18015*
[33]*Max-Planck-Institut für Physik, Munich 80805, Germany*
[34]*Michigan State University, East Lansing, Michigan 48824*
[35]*National Research Nuclear University MEPhI, Moscow 115409, Russia*
[36]*National Institute of Science Education and Research, HBNI, Jatni 752050, India*
[37]*National Cheng Kung University, Tainan 70101*
[38]*Nuclear Physics Institute of the CAS, Rez 250 68, Czech Republic*
[39]*Ohio State University, Columbus, Ohio 43210*
[40]*Institute of Nuclear Physics PAN, Cracow 31-342, Poland*
[41]*Panjab University, Chandigarh 160014, India*
[42]*Pennsylvania State University, University Park, Pennsylvania 16802*
[43]*NRC "Kurchatov Institute," Institute of High Energy Physics, Protvino 142281, Russia*
[44]*Purdue University, West Lafayette, Indiana 47907*
[45]*Rice University, Houston, Texas 77251*
[46]*Rutgers University, Piscataway, New Jersey 08854*
[47]*Universidade de São Paulo, São Paulo, Brazil 05314-970*
[48]*University of Science and Technology of China, Hefei, Anhui 230026*
[49]*Shandong University, Qingdao, Shandong 266237*
[50]*Shanghai Institute of Applied Physics, Chinese Academy of Sciences, Shanghai 201800*
[51]*Southern Connecticut State University, New Haven, Connecticut 06515*
[52]*State University of New York, Stony Brook, New York 11794*
[53]*Instituto de Alta Investigación, Universidad de Tarapacá, Chile*
[54]*Temple University, Philadelphia, Pennsylvania 19122*
[55]*Texas A&M University, College Station, Texas 77843*
[56]*University of Texas, Austin, Texas 78712*
[57]*Tsinghua University, Beijing 100084*
[58]*University of Tsukuba, Tsukuba, Ibaraki 305-8571, Japan*
[59]*United States Naval Academy, Annapolis, Maryland 21402*
[60]*Valparaiso University, Valparaiso, Indiana 46383*
[61]*Variable Energy Cyclotron Centre, Kolkata 700064, India*
[62]*Warsaw University of Technology, Warsaw 00-661, Poland*
[63]*Wayne State University, Detroit, Michigan 48201*
[64]*Yale University, New Haven, Connecticut 06520*

The STAR Collaboration at the Relativistic Heavy Ion Collider reports the first measurement of inclusive jet production in peripheral and central Au+Au collisions at $\sqrt{s_{NN}} = 200$ GeV. Jets are reconstructed with the anti-$k_T$ algorithm using charged tracks with pseudorapidity $|\eta| < 1.0$ and transverse momentum $0.2 < p_{T,\text{jet}}^{\text{ch}} < 30$ GeV/$c$, with jet resolution parameter $R = 0.2$, 0.3, and 0.4. The large background yield uncorrelated with the jet signal is observed to be dominated by statistical phase space, consistent with a previous coincidence measurement. This background is suppressed by requiring a high-transverse-momentum (high-$p_T$) leading hadron in accepted jet candidates. The bias imposed by this requirement is assessed, and the $p_T$ region in which the bias is small is identified. Inclusive charged-particle jet distributions are reported in peripheral and central Au+Au collisions for $5 < p_{T,\text{jet}}^{\text{ch}} < 25$ GeV/$c$ and $5 < p_{T,\text{jet}}^{\text{ch}} < 30$ GeV/$c$, respectively. The charged-particle jet inclusive yield is suppressed for central Au+Au collisions, compared to both the peripheral Au+Au yield from this measurement and to the $pp$ yield calculated using the PYTHIA event generator. The magnitude of the suppression is consistent with that of inclusive hadron production at high $p_T$ and that of semi-inclusive recoil jet yield when expressed in terms of energy loss due to medium-induced energy transport. Comparison of inclusive charged-particle jet yields for different values of $R$ exhibits no significant evidence for medium-induced broadening of the transverse jet profile for $R < 0.4$ in central Au+Au collisions. The measured distributions are consistent with theoretical model calculations that incorporate jet quenching.

## I. INTRODUCTION

Collisions of heavy nuclei at high energy generate a quark-gluon plasma (QGP), a state of matter with temperature and energy density similar to those of the universe a few microseconds after the Big Bang and whose dynamics are governed by the interactions of subhadronic quanta ([1] and references therein). Extensive measurements of the QGP have been carried out with nuclear collisions at the Relativistic Heavy Ion Collider (RHIC) and the Large Hadron Collider (LHC). Comparison of these measurements with theoretical calculations indicates that the QGP is an inviscid fluid exhibiting collective behavior [2]. The QGP is likewise found to be opaque to penetrating probes carrying color charge, a phenomenon known as "jet quenching" (Ref. [3] and references therein).

Jets in high-energy collisions are generated by the hard (high momentum-transfer $Q^2$) scattering of quarks and gluons (collectively, partons) from the incoming projectiles. The scattered partons fragment into correlated sprays of stable hadrons that are observed in the detector. Jet production has been measured extensively in $pp$ collisions, with theoretical calculations based on high-order perturbative quantum chromodynamics (pQCD) describing such measurements accurately over a wide kinematic range [4–8].

Jets are likewise generated in high-energy nuclear collisions, with production rates that are accurately calculable using pQCD methods [9]. Because high-$Q^2$ processes occur early in the evolution of a nuclear collision, jets probe the QGP at its highest temperature and energy density. Jet quenching, which arises from the interaction of energetic partons with the QGP via elastic and radiative processes, is expected to generate modifications in observed jet production rates and internal structure [10].

Measurement of reconstructed jets in heavy-ion collisions is challenging: A jet, which comprises ≈10 correlated particles at RHIC energies, must be distinguished from the many hundreds of particles generated by uncorrelated processes [11]. High-transverse-momentum (high-$p_T$) hadrons, which are the leading fragments of jets, can be more readily distin-

guished from this background than fully reconstructed jets. The production rate of high-$p_T$ hadrons was also predicted to be suppressed due to jet quenching [12], and suppression of inclusive production and correlations of high-$p_T$ hadrons due to jet quenching has indeed been observed at RHIC [13–20] and the LHC [21–25]. The comparison of inclusive hadron suppression measurements with theoretical calculations has been used to constrain the QGP transport parameter $\hat{q}$ [3], which characterizes the momentum transfer between a jet probe and the QGP medium.

High-$p_T$ hadron suppression provides limited insight into the mechanisms and dynamics of jet quenching, however. Observed high-$p_T$ hadrons arise predominantly from jets that have lost relatively little energy in-medium, due to the interplay of the shape of the jet-$p_T$ distribution, jet fragmentation, and jet energy loss [26–33]. The contribution to the inclusive high-$p_T$ hadron yield arising from jets undergoing significant modification due to quenching is thereby suppressed.

Broader exploration of jet quenching requires measurements with reconstructed jets. At the LHC, reconstructed-jet measurements in Pb+Pb collisions have been reported for inclusive production [34–38], correlations [39–43], and jet substructure [44–46]. At RHIC, reconstructed-jet measurements in Au+Au collisions have been reported for correlations [47,48]. While the inclusive jet and dijet production cross sections have been reported for $pp$ collisions at RHIC [4,5], the measurement of inclusive jet production in Au+Au collisions at RHIC has not been reported to date.

This paper presents the first measurement of inclusive jet production in Au+Au collisions at $\sqrt{s_{NN}} = 200$ GeV. Jets are reconstructed in central (0–10 percentile bin of the inelastic cross section) and peripheral (60–80 percentile bin) Au+Au collisions using charged tracks with transverse momentum $p_T^{\text{const}} > 0.2$ GeV/$c$ and pseudorapidity $|\eta_{\text{track}}| < 1.0$, using the anti-$k_T$ algorithm [49] with resolution parameter $R = 0.2$, 0.3, and 0.4. Uncorrelated background yield is suppressed by a cut on the leading (highest $p_T$) hadron of each jet candidate, $p_{T,\text{lead}} > p_{T,\text{lead}}^{\text{min}}$, which imposes a bias on the fragmentation

pattern of the reported jet population; we label the resulting jet population "quasi-inclusive." The effect of the bias is determined by varying the value of $p_{T,\text{lead}}^{\min}$. The distribution of the jet population arising from the large uncorrelated background is well described by a model calculation based on statistical phase space, without taking into account any multiparticle correlations whatsoever. This observation is consistent with the accurate description of the background to semi-inclusive recoil jet yields by event mixing [48].

Quasi-inclusive charged-particle jet distributions are reported in the range $5 < p_{T,\text{jet}}^{\text{ch}} < 30$ GeV/$c$ for central Au+Au collisions. Charged-particle jet yield suppression is quantified by comparing the quasi-inclusive distribution measured in central Au+Au collisions to that measured in peripheral Au+Au collisions and to the inclusive charged-particle jet distribution for $pp$ collisions generated using the PYTHIA Monte Carlo generator [50], which has been validated by comparison to inclusive measurements of pions and fully reconstructed jets at RHIC [51]. These measurements are also compared to similar inclusive jet measurements at the LHC, to semi-inclusive hadron+jet measurements at RHIC, and to theoretical calculations of jet quenching.

The paper is organized as follows: Section II describes the experiment and data selection; Sec. III presents considerations for heavy-ion jet analysis and the measurement approach; Sec. IV presents the jet reconstruction; Sec. V presents raw jet spectra; Sec. VI presents the corrections due to background fluctuations and detector effects; Sec. VII presents the systematic uncertainties; Sec. VIII presents the parametrized model (PM) and closure test; Sec. IX presents the reference spectrum from $pp$ collisions calculated using PYTHIA; Sec. X describes the theoretical calculations used for comparison; Sec. XI presents the results; and Sec. XII presents the summary.

## II. DETECTOR AND DATASET

The STAR detector is described in Ref. [52]. STAR is a large, general-purpose collider detector with high-precision tracking, particle identification, electromagnetic calorimetry, and forward detectors. The central region is immersed in a 0.5-T solenoidal magnetic field. The data for this analysis were recorded during the 2011 RHIC run with Au+Au collisions at $\sqrt{s_{NN}} = 200$ GeV. Events were selected online using a minimum bias (MB) trigger that requires signals in both forward scintillator Vertex Position Detectors (VPD), with a timing cut to constrain the primary vertex position within $|z_{\text{vtx}}| < 30$ cm of the nominal center of STAR along the beamline, and with the requirement of at least one neutron in each Zero Degree Calorimeter (ZDC), to bias toward the hadronic interaction of both Au ions. The MB trigger minimizes pileup by requiring that no additional interactions occur in a time interval of 40 $\mu$s before or after the triggered collision, consistent with the drift time of the Time Projection Chamber (TPC) [53].

Charged-particle tracks are reconstructed offline using the TPC, which has an inner radius of 50 cm and an outer radius of 200 cm, and covers the full azimuth within $|\eta_{\text{track}}| < 1$. TPC tracks have a maximum number of 45 space points.

Global tracks, which do not include the primary event vertex in the momentum fit, are accepted if they have more than 14 space points, with the ratio of the number of space points to the number of potential space points greater than 0.52. The location of the primary vertex is determined using global tracks. The primary vertex position resolution along the beam direction is 350 $\mu$m for the most central Au+Au events used in the analysis.

Jet reconstruction utilizes primary tracks, which are global tracks whose momenta have been refit with inclusion of the primary event vertex. Primary tracks with $0.2 < p_T^{\text{const}} < 30$ GeV/$c$ and which have distance of closest approach (DCA) to the primary vertex in the transverse plane DCA$_{xy} < 1$ cm are accepted for further analysis.

Events are accepted for the analysis if their reconstructed vertex lies within $|z_{\text{vtx}}| < 30$ cm of the nominal center of STAR along the beamline, and within 2 cm of the beam axis in the transverse plane. After offline event selection cuts, a total of $\approx$400 M Au+Au events were accepted, corresponding to an integrated luminosity of $\approx$6 $\mu$b$^{-1}$.

Events are classified offline in percentile bins of centrality, based on charged-particle multiplicity measured in $|\eta_{\text{track}}| < 0.5$. The accepted event population has $\approx$47 M central collision events and $\approx$94 M peripheral collision events. The online trigger efficiency is consistent with 100% for central Au+Au collisions and is approximately 70% for peripheral Au+Au collisions.

Simulated events for $pp$ collisions at $\sqrt{s} = 200$ GeV were generated using PYTHIA 6.428, tune Perugia 2012 [50]. Simulated events without instrumental effects are denoted "particle level," whereas events incorporating instrumental effects are denoted "detector level"; see Sec. VI. The largest instrumental effects in the measurement of charged-particle jets are tracking efficiency and track momentum resolution. Fast simulation events are generated by applying a $p_T$-dependent parametrization of these effects to PYTHIA-generated events.

Tracking efficiency is determined by embedding single tracks simulated at the detector level into real Au+Au events. Tracking efficiency depends on particle species; tracking efficiency for nonidentified charged tracks therefore depends on the relative population of different species. In order to assess the magnitude of this dependence, two different assumptions are made for the relative yield of charged pions, charged kaons, protons, and antiprotons comprising the charged track population: the relative yields measured in $pp$ collisions [54,55] and those measured in Au+Au collisions [55–57]. The relative yields for Au+Au collisions are used in the principal analysis, giving tracking efficiency for primary charged tracks of 68% at $p_T = 0.5$ GeV/$c$ and 72% for $p_T > 1$ GeV/$c$ in central Au+Au collisions and 85% at $p_T = 0.5$ GeV/$c$ and 88% for $p_T > 1$ GeV/$c$ in peripheral Au+Au collisions. The relative yields from $pp$ collisions give tracking efficiency that is 1% lower for $p_T < 1$ GeV/$c$, with negligible differences for $p_T > 1$ GeV/$c$. This variation is smaller than the overall systematic uncertainty assigned to the tracking efficiency, which is discussed below.

Primary track momentum resolution, which is also determined by embedding simulated tracks into real Au+Au events,

is parametrized for $p_T > 1.2$ GeV/$c$ as $\sigma_{p_T} = -0.026 + 0.020p_T + 0.003(p_T)^2$ ($p_T$ in units of GeV/$c$), with a variation $\sigma_{p_T} = 0.003(p_T)^2$ used for systematic uncertainty.

Comparison of inclusive jet spectra at different centralities requires the scaling of yields by the centrality-dependent nuclear thickness factor $\langle T_{AA} \rangle$, which is calculated using Glauber modeling [58]. In this analysis, $\langle T_{AA} \rangle$ has the value $22.8 \pm 1.6$ mb$^{-1}$ for central Au+Au collisions and $0.49 \pm 0.14$ mb$^{-1}$ for peripheral Au+Au collisions.

### III. ANALYSIS STRATEGY

Jet reconstruction algorithms provide a systematically well-controlled approach to jet measurements and corresponding theoretical calculations in $pp$ collisions at collider energies [5,7,8]. Jet measurements in heavy-ion collisions are significantly more complex, however, due to the large uncorrelated background in such events. In this section we discuss the main considerations for a theoretically interpretable measurement of the inclusive jet distribution in the large-background environment of heavy-ion collisions and the consequent strategy for this analysis.

The constituents of a jet reconstructed in a high-energy nuclear collision arise from multiple different sources, which we classify qualitatively as due to hard processes ($Q^2 >$ few GeV$^2$) or to soft processes (all others). Multiple hard processes can occur in a single nuclear collision; in the framework of QCD factorization they are considered to be incoherent. These processes can generate multiple energetic jets that overlap in $(\eta, \phi)$ space, whose hadronic fragments are thereby clustered by a jet reconstruction algorithm into a single jet candidate. Each such jet candidate will also contain copiously produced hadrons from soft processes. Jet candidates in central high-energy nuclear collisions therefore have a significant contribution from hadrons due to soft processes and may also contain hadronic fragments of one or more primordial jets arising from hard processes.

For an inclusive jet measurement in central high-energy nuclear collisions to be theoretically interpretable, it must report the distribution of a unique, well-defined jet population arising from hard processes. The measurement must therefore exclude the yield of purely combinatorial jet candidates arising solely due to contributions from soft processes, and disentangle the effects of multiple overlapping primordial jets arising from hard processes. It should also correct for the shift and smearing of the jet $p_T$ scale due to the large number of hadrons arising from soft processes in each identified hard-jet candidate.

In semi-inclusive hadron jet analyses [39,48] these corrections are implemented in three distinct steps: (i) approximate adjustment event-by-event of jet candidate $p_{T,\text{jet}}$ for the uncorrelated background contribution; (ii) rejection of background yield not correlated with the trigger, giving the raw trigger-correlated jet yield; and (iii) final correction via unfolding of the jet $p_{T,\text{jet}}$ for shift and fluctuations in the background energy density. Steps (ii) and (iii) are carried out at the level of ensemble-averaged distributions ("statistical correction"). This approach enables the measurement of trigger-normalized recoil jet distributions for large jet radius $R$ and low $p_{T,\text{jet}}$ in

the most central $A+A$ collisions, without imposing fragmentation bias on the reported jet population [39,48].

The inclusive jet distribution that is the goal of this analysis is not defined with respect to a trigger, however, and a different approach is needed for step (ii) to identify jet candidates that arise from hard processes. We therefore accept for analysis only those jet candidates whose highest-$p_T$ hadronic constituent ("leading hadron") has $p_{T,\text{lead}} > p_{T,\text{lead}}^{\min}$ [35,59]. No cut is made on $p_{T,\text{jet}}$ in this analysis, in contrast to other current measurements of inclusive jet distributions in heavy-ion collisions [34,35,37,38].

There are competing considerations for the value of $p_{T,\text{lead}}^{\min}$ [59]:

(i) The value of $p_{T,\text{lead}}^{\min}$ must be sufficiently high that the probability for such a hadron to arise from purely combinatorial jet is negligible; i.e., with high probability it is the fragment of a hard process.

(ii) The value of $p_{T,\text{lead}}^{\min}$ must be sufficiently high that the probability for multiple hadrons to satisfy this cut in a central Au+Au collision is negligible. The probability of two hard jets in an event passing this acceptance cut is therefore also negligible; with high probability there will be at most one such jet candidate in an event. This selection thereby identifies a unique, well-defined jet population arising from a specified hard process, as required.

(iii) The value of $p_{T,\text{lead}}^{\min}$ should be as low as possible to minimize the bias imposed on the accepted jet population.

The second consideration, that the value of $p_{T,\text{lead}}^{\min}$ is sufficiently high that the probability to find two such hadrons in an event is negligible, is required to ensure applicability of the correction scheme based on unfolding (Sec. VI), which is a linear transformation of a distribution that is a function of jet $p_T$.

The bias relative to the inclusive jet population imposed by the $p_{T,\text{lead}}^{\min}$ cut must be determined experimentally, for the measurement to be theoretically interpretable. The value of $p_{T,\text{lead}}^{\min}$ is consequently varied in the analysis, and the $p_{T,\text{jet}}$ range in which the corrected inclusive jet distribution does not depend significantly on $p_{T,\text{lead}}^{\min}$ is found. This is identified as the range where the bias is small.

### IV. JET RECONSTRUCTION

Jet reconstruction utilizes the $k_T$ [60] and anti-$k_T$ [49] algorithms with the boost-invariant $p_T$-recombination scheme [60], applied to all accepted charged tracks. The jet area is calculated by the Fastjet algorithm [61] with a ghost particle area of 0.01. The jet centroid is calculated as the sum of the four-vectors of its constituents [60].

This analysis employs several types of charged-particle jet, which are referred to using the notation defined in Ref. [48]: The raw transverse momentum of reconstructed jets is denoted $p_{T,\text{jet}}^{\text{raw,ch}}$, jet transverse momentum after the eventwise adjustment for uncorrelated background density is denoted $p_{T,\text{jet}}^{\text{reco,ch}}$, and jet transverse momentum after full cor-

rection for instrumental effects and background fluctuations is denoted $p_{T,\mathrm{jet}}^{\mathrm{ch}}$.

Jet reconstruction is carried out twice for each event. The first jet reconstruction pass applies the $k_T$ algorithm with $R = 0.3$ to calculate $\rho$, the estimated transverse-momentum density of background in the event [62],

$$\rho = \mathrm{median}\left\{ \frac{p_{T,\mathrm{jet}}^{\mathrm{raw},i}}{A_{\mathrm{jet}}^i} \right\}, \tag{1}$$

where index $i$ labels the charged-particle jet candidates in the event from this reconstruction pass, and $p_{T,\mathrm{jet}}^{\mathrm{raw},i}$ and $A_{\mathrm{jet}}^i$ are the transverse momentum and area of the $i$th jet. For central Au+Au collisions, the two jets with largest $p_{T,\mathrm{jet}}^{\mathrm{raw},i}$ are excluded from the median calculation, while for peripheral collisions the single jet with largest $p_{T,\mathrm{jet}}^{\mathrm{raw},i}$ is excluded. Different choices for the number of excluded jets are used for systematic variation (Sec. VII D).

The second reconstruction pass, which generates jet candidates for the measured distributions, applies the anti-$k_T$ algorithm with $R = 0.2, 0.3$, or $0.4$. Jet candidates are accepted for further analysis if their centroid lies within $|\eta_{\mathrm{jet}}| < 1 - R$, due to the TPC acceptance.

The value of $p_{T,\mathrm{jet}}^{\mathrm{raw},i}$ is adjusted according to [62]

$$p_{T,\mathrm{jet}}^{\mathrm{reco},i} = p_{T,\mathrm{jet}}^{\mathrm{raw},i} - \rho A_{\mathrm{jet}}^i, \tag{2}$$

where $i$ in this case labels the jet candidates from the second reconstruction pass and $\rho$ is determined from Eq. (1). The value of $\rho$ varies event to event: For central Au+Au collisions in this analysis, its most probable value is $31 \,\mathrm{GeV}/(c\text{-sr})$, with RMS $= 3 \,\mathrm{GeV}/(c\text{-sr})$; for peripheral Au+Au collisions its most probable value is 0, with RMS $= 1 \,\mathrm{GeV}/(c\text{-sr})$.

The definition of $\rho$ in Eq. (1) requires algorithmic choices that are not unique, including reconstruction algorithm, jet-resolution parameter $R$, and the number of jet candidates excluded from the median calculation. The adjustment to $p_{T,\mathrm{jet}}^{\mathrm{raw,ch}}$ in Eq. (2) is therefore only an estimate of the eventwise pedestal due to uncorrelated background. The absolute jet energy scale is imposed in the unfolding step described below (see also Refs. [39,48]).

Figure 1 (upper panels) show distributions of $p_{T,\mathrm{jet}}^{\mathrm{reco,ch}}$ vs. jet area in central Au+Au collisions for the inclusive charged-particle jet population without a leading particle cut (indicated by $p_{T,\mathrm{lead}}^{\mathrm{min}} = 0$; note that tracks have $p_T^{\mathrm{const}} > 0.2 \,\mathrm{GeV}/c$) with $R = 0.2$ and 0.4. Jets with small area predominantly have $p_{T,\mathrm{jet}}^{\mathrm{reco,ch}} \approx 0$. The middle and lower panels show area projections of these distributions, together with those for jets in $pp$ collisions simulated using PYTHIA with $p_{T,\mathrm{jet}}^{\mathrm{ch}} = 10$ and $20 \,\mathrm{GeV}/c$ that have been embedded into real events and for single-particle "jets" (SP, Sec. VI B). The area distributions for PYTHIA-generated and SP jets in central Au+Au collisions are similar, with negligible dependence on $p_{T,\mathrm{jet}}^{\mathrm{ch}}$. The area distributions for PYTHIA-generated and SP jets are similar in peripheral Au+Au collisions (not shown).

Figure 1 shows that, for jets with $p_{T,\mathrm{jet}}^{\mathrm{ch}} > 10 \,\mathrm{GeV}/c$, the jet area is largely a geometric quantity, with little dependence on the pattern of jet fragmentation into hadrons. The area distribution for embedded jets is peaked at $A_{\mathrm{jet}} \approx \pi R^2$, while the inclusive jet population exhibits a tail toward small area,

which arises from purely combinatorial jets without a hard component. A cut on jet area is therefore applied to suppress purely combinatorial jet candidates, while preserving high efficiency for jets that include a hard component [48]. Jet candidates are rejected if $A_{\mathrm{jet}} < 0.07$ sr for $R = 0.2$, $A_{\mathrm{jet}} < 0.2$ sr for $R = 0.3$, and $A_{\mathrm{jet}} < 0.4$ sr for $R = 0.4$.

## V. UNCORRECTED JET DISTRIBUTIONS

Figure 2 shows measured $p_{T,\mathrm{jet}}^{\mathrm{reco,ch}}$ distributions for inclusive jet candidates with $R = 0.2, 0.3$, and 0.4, which pass the jet area cut, in peripheral and central Au+Au collisions. The distributions for central Au+Au collisions have significant yield in the region $p_{T,\mathrm{jet}}^{\mathrm{reco,ch}} < 0$. This feature is also observed in hadron-triggered semi-inclusive analyses [39,48], where it is attributed predominantly to combinatorial jet candidates generated by soft processes that are uncorrelated with the trigger.

The distributions exhibit a change in slope at $p_{T,\mathrm{jet}}^{\mathrm{reco,ch}} \approx 10 \,\mathrm{GeV}/c$ for all $R$ in peripheral Au+Au collisions, and at $p_{T,\mathrm{jet}}^{\mathrm{reco,ch}} \approx 15 \,\mathrm{GeV}/c$ for $R = 0.2$ in central Au+Au collisions, suggesting two distinct contributions to the spectrum that are visible for the configurations with smallest background. In this picture the yield at low $p_{T,\mathrm{jet}}^{\mathrm{reco,ch}}$ is dominated by combinatorial jet candidates, similarly to distributions in the hadron+jet analysis, while the yield at large $p_{T,\mathrm{jet}}^{\mathrm{reco,ch}}$ is dominated by jets arising from hard processes.

Figure 3 shows the effect of the cut $p_{T,\mathrm{lead}} > p_{T,\mathrm{lead}}^{\mathrm{min}}$ on $p_{T,\mathrm{jet}}^{\mathrm{reco,ch}}$ distributions in peripheral and central Au+Au collisions. The $p_{T,\mathrm{lead}}^{\mathrm{min}}$ cut suppresses the yield most strongly for large negative values of $p_{T,\mathrm{jet}}^{\mathrm{reco,ch}}$, with much reduced suppression at large positive values of $p_{T,\mathrm{jet}}^{\mathrm{reco,ch}}$.

Larger values of $p_{T,\mathrm{lead}}^{\mathrm{min}}$ generate larger suppression, with correspondingly larger bias expected in the fully corrected distributions. Section III specifies the competing criteria for optimizing the value of $p_{T,\mathrm{lead}}^{\mathrm{min}}$. The optimum value of $p_{T,\mathrm{lead}}^{\mathrm{min}}$ for this analysis is found to be $p_{T,\mathrm{lead}}^{\mathrm{min}} = 5 \,\mathrm{GeV}/c$, which is the lowest value that gives stable unfolding results (Sec. VI C) and successful closure (Sec. VIII). The value $p_{T,\mathrm{lead}}^{\mathrm{min}} = 7 \,\mathrm{GeV}/c$ is used for systematic variation, to determine the range in $p_{T,\mathrm{jet}}^{\mathrm{ch}}$ over which the bias is small (Sec. XI).

## VI. CORRECTIONS

The raw distributions are corrected for the effects of instrumental response and background fluctuations, using regularized unfolding [63–65]. We utilize the approach and notation described in Ref. [48].

### A. Instrumental response matrix $R_{\mathrm{det}}$

The instrumental response matrix $R_{\mathrm{det}}$ is constructed using PYTHIA-generated events for $pp$ collisions at $\sqrt{s} = 200$ GeV. A detector-level event is generated by applying the fast simulator to each particle-level event. Jet reconstruction is then carried out with the anti-$k_T$ algorithm at both the particle and detector levels, and jets are selected by applying the fiducial acceptance ($|\eta_{\mathrm{jet}}| < 1 - R$) and $p_{T,\mathrm{lead}}^{\mathrm{min}}$ cuts. Jets
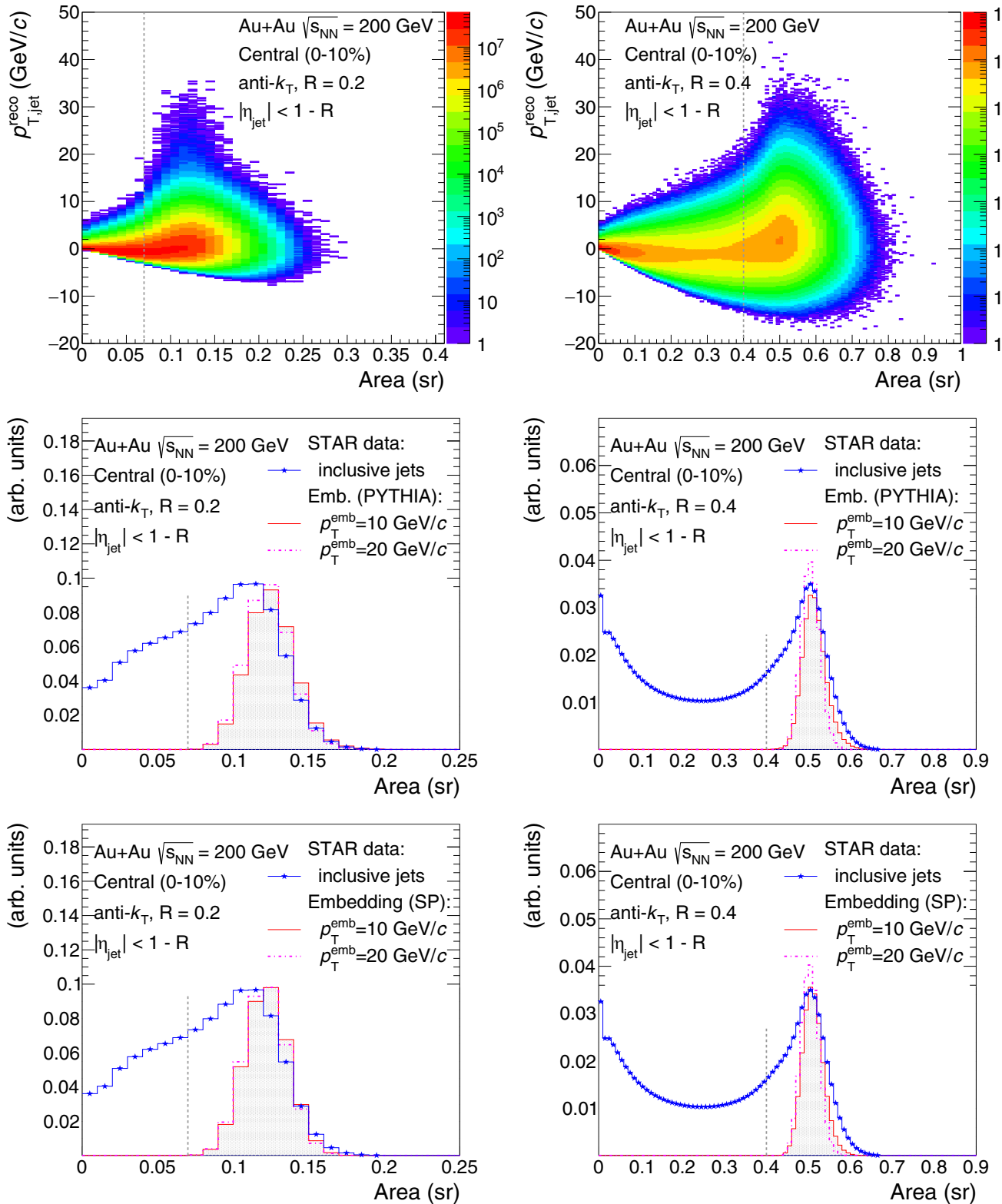
FIG. 1. Distribution of $p_{T,\mathrm{jet}}^{\mathrm{reco,ch}}$ and jet area for the inclusive charged-particle jet population ($p_{T,\mathrm{lead}}^{\min} = 0$) in central Au+Au collisions. Upper panels: $p_{T,\mathrm{jet}}^{\mathrm{reco,ch}}$ vs. jet area for $R = 0.2$ (left) and $R = 0.4$ (right). Middle and lower panels: Projection onto the jet area axis. Also shown are area distributions for PYTHIA-generated (middle) and SP jets (lower) with $p_T^{\mathrm{emb}} = 10$ and $20$ GeV/$c$, embedded into real Au+Au data for central collisions. The vertical dashed lines show the jet area cut.

FIG. 2. Distribution of inclusive charged-particle jet candidates passing the jet area cut as a function of $p_{T,\text{jet}}^{\text{reco,ch}}$ for $R = 0.2$, 0.3, and 0.4, in peripheral (upper) and central (lower) Au+Au collisions.

at the particle and detector levels are matched following the procedure in Ref. [48]: Tracks are first matched at the detector and particle levels, and then the detector-level jet with the largest fraction of the energy of a given particle-level jet is matched to it, if that fraction is greater than 50%.

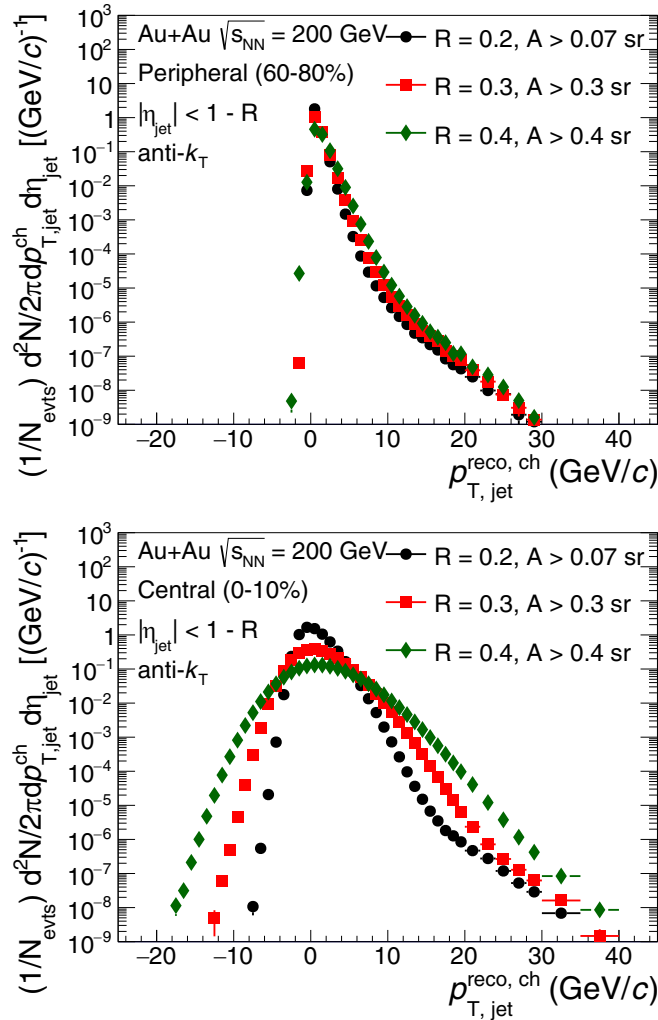The instrumental response is determined by comparing matched jets at the particle and detector levels. Figure 4 shows the distribution of $p_{T,\text{jet}}^{\text{det}}$ for u-quark-initiated jets with several values of $p_{T,\text{jet}}^{\text{part}}$, with detector-level effects corresponding to those for central Au+Au collisions. The cut $p_{T,\text{lead}}^{\min} = 5$ GeV/$c$ is applied both at the particle and detector levels for the primary analysis, with $p_{T,\text{lead}}^{\min} = 7$ GeV/$c$ used to correct the corresponding analysis used for systematic variation (not shown). The distributions for gluon-initiated jets are very similar, suggesting that the instrumental response does not depend significantly on the specific mixture of light quark- and gluon-initiated jets in the population.

The instrumental response in Fig. 4 is asymmetric, with a tail for $p_{T,\text{jet}}^{\text{det}} < p_{T,\text{jet}}^{\text{part}}$ that arises predominantly from the

loss of a single charged hadron with high momentum-fraction (high-$z$) due to tracking inefficiency [48]. This asymmetric response cannot be characterized fully by a Jet Energy Resolution (JER) figure, and so the entire distribution shown in Fig. 4 is used to correct the spectrum for instrumental effects. Nevertheless, as an approximation to the JER, we fit the main peak of these distributions with a Gaussian function and report its relative width, as shown in the figure. For jets with $7 < p_{T,\text{jet}}^{\text{part}} < 40$ GeV/$c$, the relative width has values between 4 and 10%, with negligible dependence on fragmentation model or jet resolution parameter $R$.

A detector-level jet corresponding to a particle-level jet in the experimental acceptance can be lost due to fiducial cuts and instrumental response. The most significant contribution to this loss is tracking inefficiency, especially for low-$p_T$ jets containing few tracks. The jet area cut has negligible inefficiency for $p_{T,\text{jet}}^{\text{part}} > 4$ GeV/$c$.

For transparency in understanding the effects of unfolding, corrections for $p_T$ smearing and jet finding efficiency are applied in separate steps. This is implemented by normalizing the elements of $R_{\text{det}}$ such that, for each bin in $p_{T,\text{jet}}^{\text{part}}$, the integral over $p_{T,\text{jet}}^{\text{det}}$ is unity; $R_{\text{det}}$ thereby only corrects for $p_T$ smearing. The effects of jet finding efficiency are then corrected by multiplying the unfolded solution with the efficiency as a function of $p_{T,\text{jet}}^{\text{part}}$.

Figure 5 shows the jet reconstruction efficiency. The nominal calculation is carried out for a mixture of u-quark and gluon jets with yield ratio 2:1, and the nominal tracking efficiency. The efficiencies for pure u-quark or gluon populations are also shown, as is the jet-finding efficiency for $\pm$ 5% relative variation in tracking efficiency, corresponding to its systematic uncertainty. The single-track efficiency is also shown, which corresponds to the jet reconstruction efficiency for $p_{T,\text{jet}}^{\text{part}} = p_{T,\text{lead}}^{\min}$.

A particle-level jet without a sufficiently hard leading track may be accepted at the detector-level due to track momentum smearing. This jet feed-up increases the jet finding efficiency for the lowest $p_{T,\text{jet}}$ values by 1–2% (absolute). Figure 5 includes this effect.

A track from a displaced vertex arising from a weak decay may be assigned an incorrect momentum that situates it inside or outside of a jet cone differently than its parent particle. However, such effects are found to be negligible [48] and no correction for them is applied.

Figure 6 (left panel) shows the matrix $R_{\text{det}}$ for central Au+Au collisions. Contributions in the region $p_{T,\text{jet}}^{\text{det}} < p_{T,\text{jet}}^{\text{part}}$ are due primarily to tracking efficiency, which causes tracks to be lost from the jet. Contributions in the region $p_{T,\text{jet}}^{\text{det}} > p_{T,\text{jet}}^{\text{part}}$, which are less probable, arise primarily from the effect of momentum resolution for cases in which the fraction of $p_{T,\text{jet}}$ lost due to tracking inefficiency is small.

The Jet Energy Scale (JES) uncertainty due to instrumental effects, which is dominated by the uncertainty of the tracking efficiency, is $\approx 5\%$ for $R = 0.2$ and 0.3, and 7% for $R = 0.4$, in central Au+Au collisions; and 3% for $R = 0.2$, 0.3, and 0.4 in peripheral Au+Au collisions. The dependence of JES on $p_{T,\text{jet}}^{\text{det}}$ is negligible.
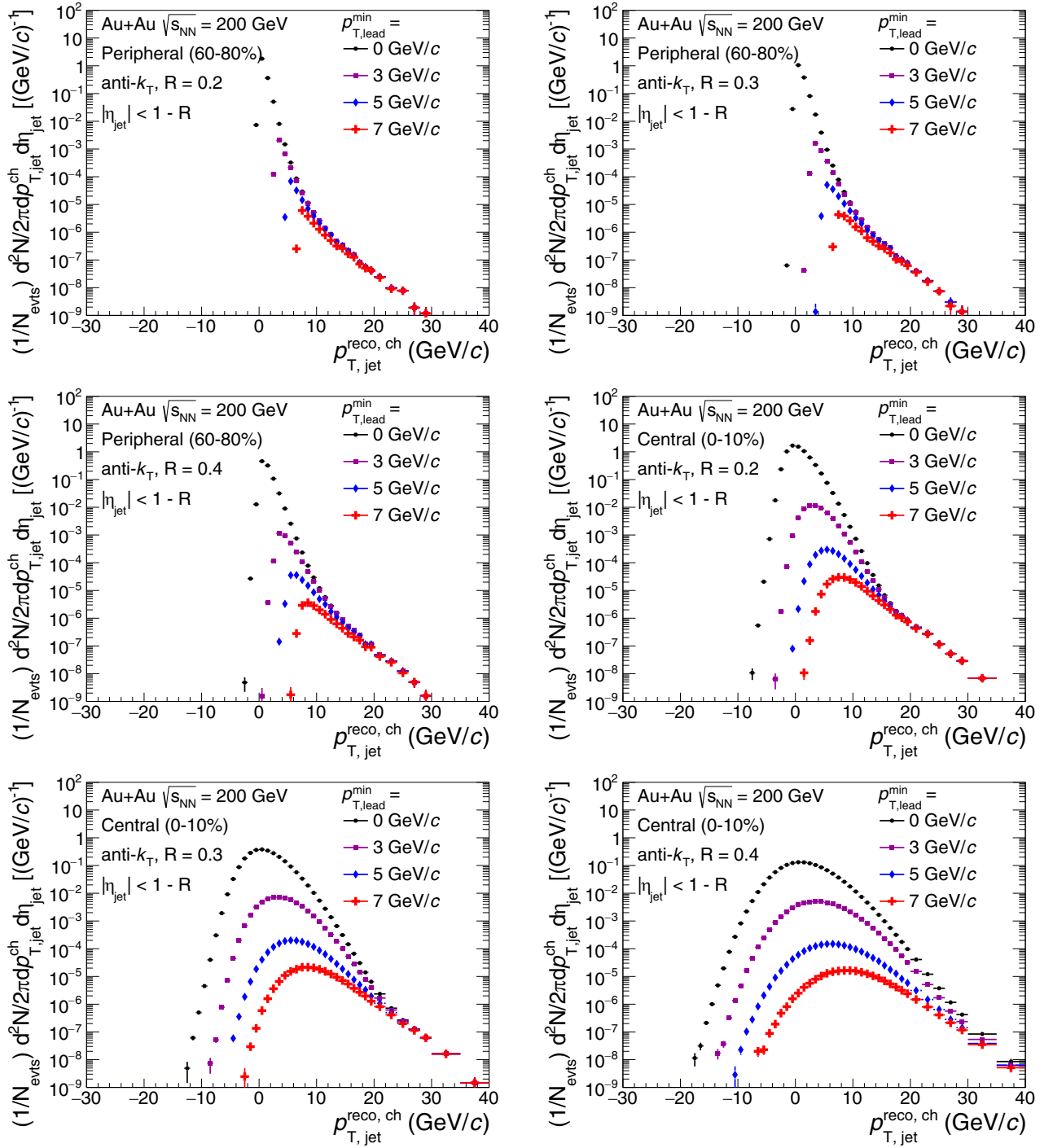
FIG. 3. Distribution of $p_{T,\mathrm{jet}}^{\mathrm{reco,ch}}$ measured in peripheral (left) and central (right) Au+Au collisions at $\sqrt{s_{NN}} = 200$ GeV, for $p_{T,\mathrm{lead}}^{\mathrm{min}} = 0, 3, 5,$ and 7 GeV/$c$. Upper: $R = 0.2$; middle: $R = 0.3$; lower: $R = 0.4$. The distributions for $p_{T,\mathrm{lead}}^{\mathrm{min}} = 0$ are the same as those in Fig. 2.

## B. Uncorrelated background response matrix $R_{\mathrm{bkg}}$

The response matrix representing fluctuations in energy density uncorrelated with a jet arising from a hard process is calculated by embedding detector-level simulated jets into real events, reconstructing the hybrid events, and then matching each embedded jet with a reconstructed jet. The matching of particle- and detector-level jets likewise follows the procedure in Ref. [48]. The response matrix corresponds to the probabil-

ity distribution for $\delta p_T$, where

$$\delta p_T = p_{T,\mathrm{jet}}^{\mathrm{reco,ch}} - p_T^{\mathrm{emb}}. \qquad (3)$$

Jet reconstruction algorithms are infrared and collinear-safe (IRC-safe) in elementary collision systems, i.e., they measure energy flow and are insensitive to the specific pattern of jet fragmentation into hadrons. In this analysis we likewise seek to measure energy flow for charged-particle jets
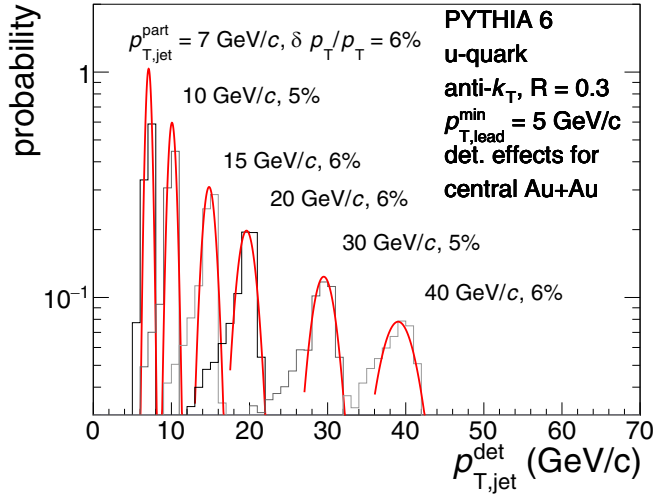
FIG. 4. Instrumental jet response: Distribution of $p_{T,\text{jet}}^{\text{det}}$ for u-quark jets generated by PYTHIA with various values of $p_{T,\text{jet}}^{\text{part}}$, with detector effects corresponding to those in central Au+Au collisions. Jets have $R = 0.3$ and are selected with the requirement $p_{T,\text{lead}}^{\text{min}} = 5$ GeV/$c$ at both the particle and detector levels. The red distributions show a Gaussian functional fit to the peak region of each distribution, with relative width of the fit as shown.

in heavy-ion collisions, without bias toward specific patterns of jet fragmentation. That goal requires the $\delta p_T$ distribution not to have significant dependence on the jet fragmentation pattern.

In order to test this dependence, we calculate the $\delta p_T$ distribution in Eq. (3) with two significantly different jet fragmentation models: light quark jets generated by PYTHIA (PYlq), utilizing the PYTHIA fragmentation routines for a quark of specified flavor and momentum; and "single-particle" jets (SP), in which the entire jet $p_T$ is carried by a single hard particle [66]. Figure 7 (upper panels) compare the $\delta p_T$ probability distributions for the SP and PYlq fragmentation models for $R = 0.2$ and 0.4 jets with $p_{T,\text{jet}}^{\text{ch}} = 20$ GeV/$c$ embedded into central Au+Au collisions; the cut $p_{T,\text{lead}}^{\text{min}} = 5$ GeV/$c$ is applied to the PYlq jets. The two fragmentation models generate similar $\delta p_T$ distributions, having similar shape and differing by a shift of $\approx 500$ MeV. This variation is accounted for in the systematic uncertainty, discussed below. Figure 1 shows that the jet area distributions for these two fragmentation models are also similar.

Figure 6 (middle panel) shows the background response matrix $R_{\text{bkg}}$, whose elements are the $\delta p_T$ probability distribution as a function of $p_{T,\text{jet}}$, calculated by SP embedding.

High-$p_T$ hadrons may be correlated in azimuth with the event plane (EP) orientation [67]. The strength of this correlation is characterized by $v_2$, the second-order Fourier coefficient of the azimuthal distribution between the hadron and the EP. Nonzero $v_2$ for hadrons with $p_T > p_{T,\text{lead}}^{\text{min}}$ will bias the orientation of the accepted jet population relative to the EP, thereby biasing the level of uncorrelated background. This bias is taken into account in the calculation of the $\delta p_T$ probability distribution by weighting each embedded jet with
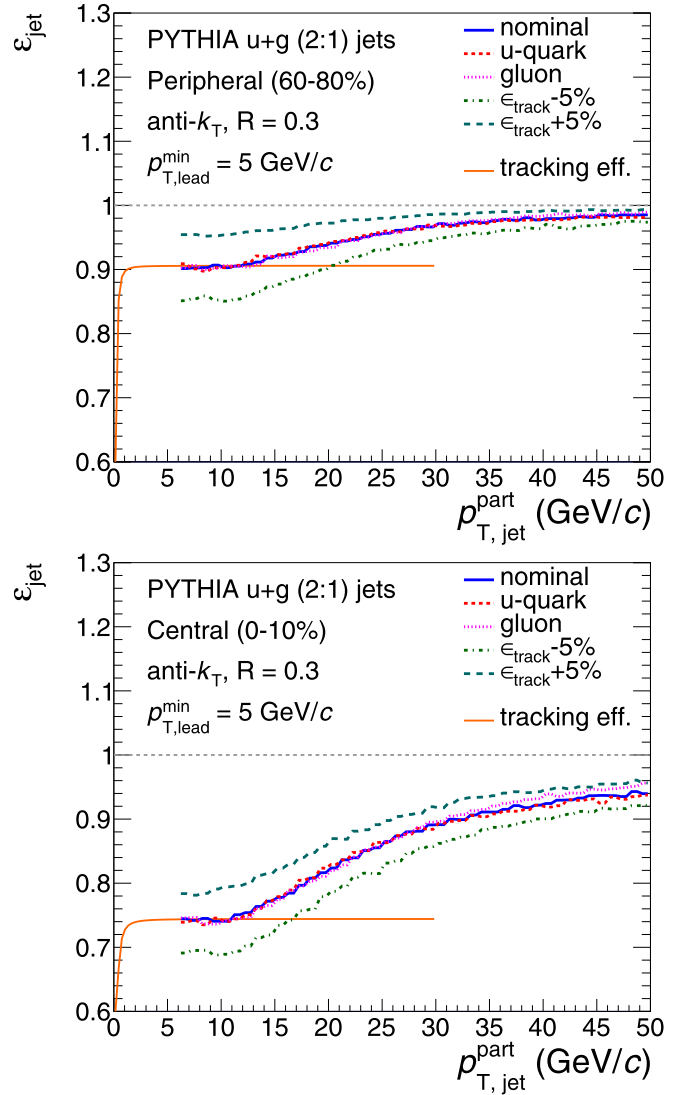




FIG. 5. Jet reconstruction efficiency in peripheral (upper) and central (lower) Au+Au collisions, for $R = 0.3$ and $p_{T,\text{lead}}^{\text{min}} = 5$ GeV/$c$, for u quarks and gluons in the ratio 2:1 (labeled "nominal"), pure u, pure g, and variation of the relative tracking efficiency by $\pm 5\%$ for the nominal population. The orange line shows the single-track efficiency.

a weight $w$,

$$w = 1 + 2v_2 \cos(2\Delta\phi), \tag{4}$$

where $\Delta\phi$ is the azimuthal angle of the leading hadron relative to the EP axis. Figure 7 (upper panels) show $\delta p_T$ probability distributions with SP embedding for $p_{T,\text{jet}} = 20$ GeV/$c$, for $v_2 = 0$ and for $v_2 = 0.04$, with the latter value consistent with hadron $v_2$ measured in the region $p_T > p_{T,\text{lead}}^{\text{min}}$ [67]. This variation in $v_2$ is seen to generate negligible variation in the $\delta p_T$ distributions, and its effect is likewise negligible in the final corrected spectra. This is the only contribution of azimuthal asymmetry effects to the analysis.

Figure 7 (lower panels) show $\delta p_T$ probability distributions for SP jets with embedded $p_{T,\text{jet}} = 5, 10$, and 20 GeV/$c$. These
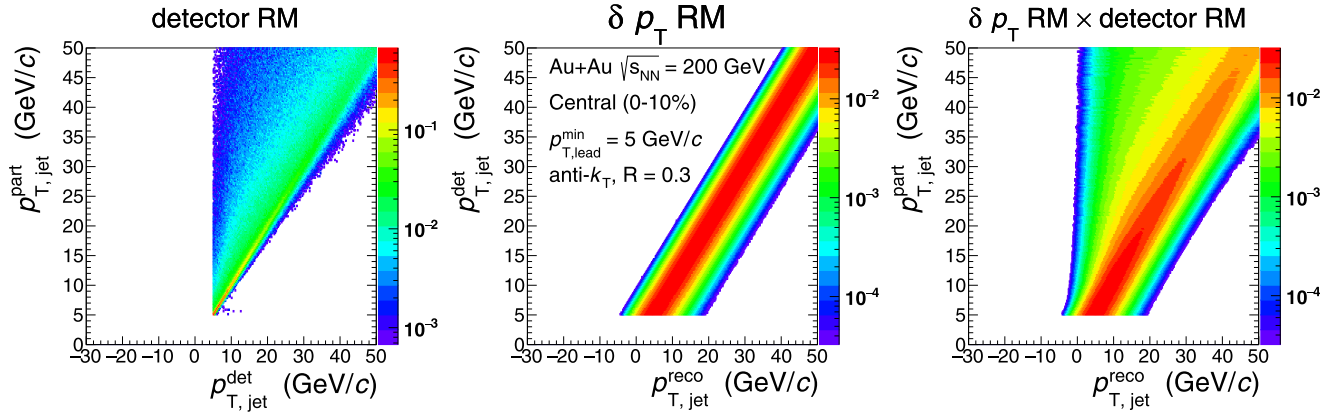
FIG. 6. Response matrices (RM) for charged jets with $p_{T,\text{lead}}^{\min} = 5$ GeV/$c$ and $R = 0.3$. Left: Detector effects $R_{\text{det}}$; center: background fluctuations $R_{\text{bkg}}$ (SP embedding); right: $R_{\text{total}} = R_{\text{bkg}} \times R_{\text{det}}$.
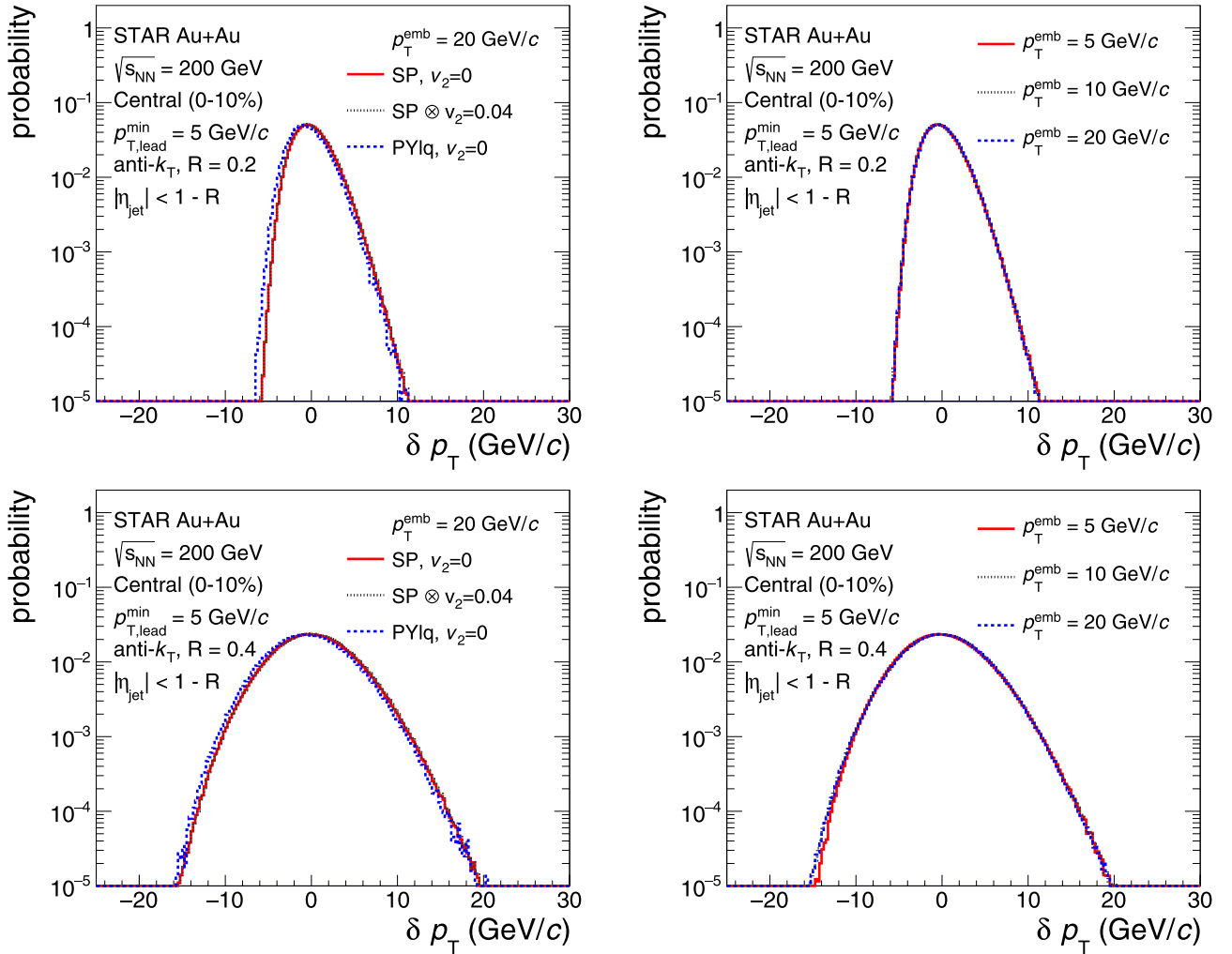


FIG. 7. $\delta p_T$ distributions calculated by embedding various types of simulated jet in central Au+Au collisions at $\sqrt{s_{NN}} = 200$ GeV, for $R = 0.2$ (left) and $R = 0.4$ (right). Upper panels: $p_T^{\text{emb}} = 20$ GeV/$c$ for SP jets, SP jets with $v_2$-modulated background, and light quark jets generated by PYTHIA. Lower panels: SP jets for several values of $p_T^{\text{emb}}$. See text for details.

distributions exhibit negligible dependence on $p_{T,\text{jet}}$ for $R = 0.2$, and minor dependence for $R = 0.4$.

Figure 7 shows that the response matrix for background fluctuations in central Au+Au collisions is largely independent of both $p_{T,\text{jet}}$ and the fragmentation model used in the calculation. A similar lack of dependence on fragmentation model is found for peripheral Au+Au collisions. This indicates that jet reconstruction in this analysis indeed measures energy flow within jets, as required. The small residual variations seen in Fig. 7 are taken into account in the systematic uncertainty of the corrected spectra.

### C. Unfolding

The unfolding procedure utilizes the cumulative response matrix [Fig. 6 (right panel)], which is the product of $R_{\text{bkg}}$ and $R_{\text{det}}$. Two different unfolding methods are used: an iterative method based on Bayes's theorem [68], and a method based on singular value decomposition (SVD) [64].

Several different functional forms are used for the prior distribution: a power-law distribution, $p_T^{-n}$, with $n = 4.5, 5.0$, and 5.5; the inclusive jet distribution generated by PYTHIA for $pp$ collisions at $\sqrt{s} = 200$ GeV, with $p_{T,\text{lead}}^{\min} = 5$ GeV/$c$; and the Tsallis function [48,69], with $n$ varying between 4 and 20 and $T$ varying between 0.6 and 1.2.

The unfolding procedure is regularized, which imposes a smoothness constraint on the solution [63–65]. The back-folded distribution, which is the unfolded distribution smeared by the response matrix, is used to optimize the regularization. For iterative Bayesian unfolding, regularization corresponds to limiting the number of iterations $i$; optimization of the regularization is based on comparison of unfolded distributions for two successive iterations, and comparison of the backfolded and uncorrected distributions. For SVD unfolding, regularization corresponds to truncation of the expansion at $k$ terms; optimization of the value of $k$ is determined by comparing the backfolded and uncorrected distributions.

Values of $i$ or $k$ are accepted if the distance between the unfolded and backfolded histogram (or between successive iterations in the case of $i$) is sufficiently small. The histogram distance is quantified using the average relative distance between the central values of two distributions $a$ and $b$,

$$d_{\text{rel}} = \frac{1}{n} \sum_{i=1}^{n} \frac{|a_i - b_i|}{\min(a_i, b_i)}, \qquad (5)$$

where $n$ is the number of bins and $a_i$ and $b_i$ denote the central values in bin $i$.

This approach is based on PM simulations (Sec. VIII) which show that a small distance between backfolded and unfolded solutions, or between successive iterations for Bayesian unfolding, corresponds to a small distance between the unfolded and generated spectra. The $d_{\text{rel}}$ metric is found to provide better discrimination than $\chi^2$ and Kolmogorov-Smirnov metrics.

### D. Magnitude of corrections

In this section we estimate the magnitude of corrections to the quasi-inclusive jet spectrum, to provide context for
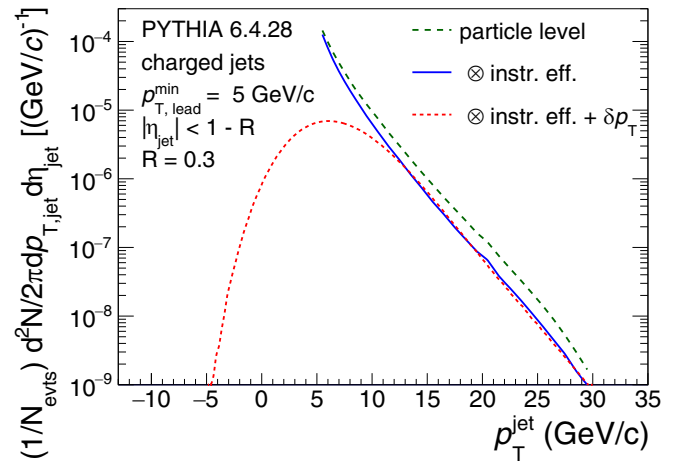


FIG. 8. Estimated magnitude of corrections for charged jets with $R = 0.3$ and $p_{T,\text{lead}}^{\min} = 5.0$ GeV/$c$, for central Au+Au collisions. See text for details.

the systematic uncertainties discussed below. This estimate utilizes PYTHIA-generated events for $pp$ collisions at $\sqrt{s} = 200$ GeV, with instrumental effects corresponding to central Au+Au collisions. The detector-level spectrum is smeared to account for background fluctuations and is scaled by $\langle T_{AA} \rangle$, likewise for central Au+Au collisions.

Figure 8 shows the results of this calculation: the distribution of charged jets with $R = 0.3$ and $p_{T,\text{lead}}^{\min} = 5.0$ GeV/$c$ at the particle level (green dashed line), which is modified cumulatively by instrumental effects (blue solid line) and background fluctuations ($\delta_{p_T}$, red dashed). Correction by unfolding for this case corresponds to transforming the red-dashed to the green-dashed distribution. At fixed values of $p_{T,\text{jet}}$, the effect of the unfolding correction for $p_{T,\text{jet}}^{\text{ch}} > 15$ GeV/$c$ is a factor $\approx 2$ in yield, while the yield correction at lower $p_{T,\text{jet}}^{\text{ch}}$ is significantly larger, due predominantly to the effect of background fluctuations that transport yield to the region $p_{T,\text{jet}}^{\text{ch}} < 0$.

## VII. SYSTEMATIC UNCERTAINTIES

Systematic uncertainties arise from corrections for instrumental response and background fluctuations, and from the unfolding procedure. We distinguish two categories of systematic uncertainty: correlated uncertainties, which do not change the shape of the distribution, and shape uncertainties.

Table I shows the significant contributions to the systematic uncertainty. For each component, the corresponding contribution to the response matrix is varied and the full correction procedure was carried out. The resulting variation in the corrected spectrum gives the systematic uncertainty due to that component.

### A. Tracking

The largest instrumental uncertainty is due to tracking efficiency ("tracking efficiency" Table I), whose relative uncertainty is $\pm 5\%$ [70].

TABLE I. Components of the systematic uncertainty (%) for jets with $R = 0.2$, 0.3, and 0.4 in central and peripheral Au+Au collisions. See text for details.

| | | Central Au+Au collisions, $\sqrt{s_{NN}}=200$ GeV | | | | | | Peripheral Au+Au collisions, $\sqrt{s_{NN}}=200$ GeV | | | | | |
|---|---|---|---|---|---|---|---|---|---|---|---|---|---|
| | $R$ | 0.2 | | 0.3 | | 0.4 | | 0.2 | | 0.3 | | 0.4 | |
| | $p_{T,\mathrm{jet}}^{\mathrm{ch}}$ (GeV/$c$) | [14,16] | [20,25] | [14,16] | [20,25] | [14,16] | [20,25] | [14,16] | [18,20] | [14,16] | [18,20] | [14,16] | [18,20] |
| **Correlated** | Tracking efficiency | $^{+15}_{-12}$ | $^{+16}_{-10}$ | $^{+16}_{-13}$ | $^{+12}_{-22}$ | $^{+14}_{-11}$ | $^{+18}_{-12}$ | $^{+6}_{-8}$ | $^{+10}_{-12}$ | $^{+12}_{-11}$ | $^{+14}_{-12}$ | $^{+13}_{-12}$ | $^{+16}_{-12}$ |
| | Fragmentation for $R_{\mathrm{det}}$ | $^{+1}_{-3}$ | $^{+3}_{-1}$ | $^{+3}_{-1}$ | $^{+4}_{-5}$ | $^{+4}_{-1}$ | $^{+12}_{-2}$ | $^{+0}_{-5}$ | $^{+0}_{-5}$ | $^{+0}_{-1}$ | $^{+2}_{-2}$ | $^{+2}_{-1}$ | $^{+3}_{-1}$ |
| | $\delta p_T$ | $^{+8}_{-3}$ | $^{+16}_{-1}$ | $^{+10}_{-2}$ | $^{+17}_{-2}$ | $^{+7}_{-5}$ | $^{+14}_{-3}$ | $^{+10}_{-1}$ | $^{+15}_{-1}$ | $^{+9}_{-1}$ | $^{+11}_{-1}$ | $^{+8}_{-1}$ | $^{+11}_{-1}$ |
| | $\rho$ | $^{+1}_{-1}$ | $^{+1}_{-1}$ | $^{+1}_{-0}$ | $^{+0}_{-1}$ | $^{+1}_{-1}$ | $^{+1}_{-1}$ | $^{+1}_{-3}$ | $^{+4}_{-1}$ | $^{+1}_{-3}$ | $^{+2}_{-4}$ | $^{+1}_{-3}$ | $^{+1}_{-4}$ |
| | **Total correlated** | $^{+17}_{-13}$ | $^{+24}_{-10}$ | $^{+19}_{-13}$ | $^{+21}_{-23}$ | $^{+17}_{-11}$ | $^{+26}_{-13}$ | $^{+12}_{-10}$ | $^{+18}_{-14}$ | $^{+15}_{-11}$ | $^{+18}_{-13}$ | $^{+15}_{-12}$ | $^{+20}_{-13}$ |
| **Shape** | Unfolding | $^{+17}_{-14}$ | $^{+12}_{-10}$ | $^{+24}_{-19}$ | $^{+25}_{-18}$ | $^{+46}_{-29}$ | $^{+51}_{-31}$ | $^{+14}_{-11}$ | $^{+8}_{-7}$ | $^{+8}_{-6}$ | $^{+17}_{-12}$ | $^{+4}_{-3}$ | $^{+11}_{-9}$ |

### B. Fragmentation model for $R_{\mathrm{det}}$

The calculation of $R_{\mathrm{det}}$ incorporates a fragmentation model to determine the instrumental response to a jet. The primary analysis utilizes a relative population of light quarks and gluons in the ratio 2:1 at all $p_{T,\mathrm{jet}}^{\mathrm{det}}$. Systematic variations utilize 100% light quark or 100% gluon fragmentation. The corresponding entry in Table I is labeled "fragmentation for $R_{\mathrm{det}}$."

### C. $\delta p_T$ for $R_{\mathrm{bkg}}$

The primary analysis utilizes SP jets to calculate $\delta p_T$. For systematic variation, $\delta p_T$ distributions are calculated utilizing PYTHIA-generated fragmentation for light-quark jets. The requirement that accepted jets have $p_{T,\mathrm{lead}}^{\mathrm{min}} = 5$ GeV/$c$ biases the background distribution, since hadrons with $p_T > 5$ GeV/$c$ may be correlated in azimuth with the EP [Eq. (4)]. The primary analysis utilizes $v_2 = 0.04$, which is the maximum value compatible with the current measurement [67], while $v_2 = 0$ is used for systematic variation. The corresponding entry in Table I is labeled "$\delta p_T$."

### D. Median background density $\rho$

The calculation of $\rho$ [Eq. (1)] is varied relative to that for the primary analysis by using $R = 0.2$ or 0.4 for the first jet reconstruction pass, or by excluding only the single most energetic jet for central Au+Au collisions and no jets for peripheral Au+Au collisions. The corresponding entry in Table I is labeled "$\rho$."

### E. Unfolding

Systematic variation of the unfolding procedure corresponds to variation of its components: algorithm, prior distribution, and regularization criterion. The components are varied independently and the unfolding procedure is carried out for each such variant. The unfolded solution from a variant is accepted if it satisfies the same quality criteria as those used in the primary analysis (see Sec. VI C).

The algorithm is varied by using the Bayesian and SVD approaches. Variation of the prior distribution is discussed in Sec. VI C. Variation of the regularization parameter corresponds to variation of the number of iterations $i$ for Bayesian unfolding and the number of terms $k$ in the series expansion

for SVD unfolding: Both $i$ and $k$ were increased by 1 relative to their optimum values found in the primary analysis.

For each bin in $p_{T,\mathrm{jet}}^{\mathrm{ch}}$, the central value of the reported distribution is the mean of all accepted unfolded distributions from this variation procedure. The systematic uncertainty due to unfolding is the corresponding RMS, calculated separately for positive and negative excursions relative to the mean; the resulting uncertainty is therefore asymmetric. The corresponding entry in Table I is labeled "unfolding."

### F. $\langle T_{AA} \rangle$

The uncertainties of the nuclear thickness factor $\langle T_{AA} \rangle$ are specified in Sec. II.

### G. Cumulative uncertainty

The total correlated systematic uncertainty in Table I is the quadrature sum of the individual component contributions for each bin in $p_{T,\mathrm{jet}}^{\mathrm{ch}}$. The most significant sources of systematic uncertainty in both peripheral and central collisions are the unfolding procedure, tracking efficiency, and the choice of $\delta p_T$ probe. Other uncertainty sources generate smaller contributions.

## VIII. PARAMETRIZED MODEL AND CLOSURE TEST

The contribution of uncorrelated background to semi-inclusive hadron+jet distributions in central Au+Au collisions at $\sqrt{s_{NN}} = 200$ GeV is well described by a mixed-event population [48]. This indicates that such background distributions are largely statistical in nature, with dynamically generated correlations having small or negligible influence. In this paper we explore a related approach to describe the uncorrelated background to the inclusive jet distribution, utilizing a PM calculation that accurately describes the eventwise distributions of mean-$p_T$ ($\langle p_T \rangle$) and mean transverse energy ($\langle E_T \rangle$) in high-energy nuclear collisions [71–73] (see also Refs. [74–77]). We apply this model in a closure test of this analysis, which assesses the precision with which a known signal is reproduced by the full measurement procedure.

For trigger-normalized coincidence measurements, a closure test can be carried out by embedding simulated signal pairs into real events, reconstructing the hybrid event, and

executing the full analysis chain [48]. If the rate per real event of the process of interest is much less than unity, identification of the embedded signal trigger can be made without significant ambiguity in such a procedure. In contrast, for an inclusive jet analysis, the jet distribution is normalized per event, not per trigger, and such an embedding procedure effectively modifies the inclusive jet distribution found in real events. The closure test in this approach then corresponds to measuring this modification. The modification is, however, not well defined, since the intrinsic jet spectrum of real events is unknown in central Au+Au collisions; indeed, measuring it is the goal of the analysis. A different approach to the closure test is therefore required for inclusive jet distributions.

The inclusive jet measurement closure test therefore requires the analysis of fully simulated events, whose global properties mimic those of Au+Au collisions and whose inclusive jet distribution is known by construction. One approach for the closure test is to generate events using established Monte Carlo event generators such as HIJING [78] or PYQUEN [79], which reproduce the global features of heavy-ion collisions at RHIC and the LHC. However, the statistical precision of a meaningful closure test must be similar to that of the real data analysis, which is difficult to achieve with such MC calculations. We therefore utilize events generated by the PM, which is computationally more efficient than MC generators, and which likewise reproduces the global properties of Au+Au collisions at $\sqrt{s_{NN}} = 200$ GeV and has a specified inclusive jet distribution. Comparison of the PM calculation with data has the additional benefit of providing insight into the nature of the backgrounds in this measurement.

The following considerations motivate a statistical approach to modeling the background in this analysis. Eventwise distributions of $\langle p_T \rangle$ and $\langle E_T \rangle$ in limited acceptance have been measured in high-energy nuclear collisions [71–77]. These distributions are well-described by mixed-event analyses [71,73–76], and by calculations based on uncorrelated particle emission [71–73,80]. The uncorrelated background in semi-inclusive hadron+jet distributions at $\sqrt{s_{NN}} = 200$ GeV is likewise well reproduced by a mixed-event approach [48], showing that the background distribution in heavy-ion jet measurements is predominantly statistical, with dynamically generated correlations on the scale of the resolution parameter $R$, due to jets and other QCD mechanisms, playing a smaller, even negligible, role.

In the PM, hadrons are generated from two sources [59]: a soft physics component based on uncorrelated particle emission and the production and fragmentation of hard jets based on a PYTHIA calculation for $pp$ collisions. All generated "hadrons" are identical, with zero mass and charge.

The soft hadronic component comprises $M$ independent particles distributed uniformly in azimuth ($0 < \varphi < 2\pi$) and pseudorapidity ($|\eta| < 1$), and distributed in $p_T$ according to a Boltzmann function,

$$\frac{dN_{\text{soft}}^{AA}}{dp_T} \propto \frac{4p_T}{\langle p_T \rangle^2} e^{-2p_T/\langle p_T \rangle}, \qquad (6)$$

where the parameters $\langle p_T \rangle$ and $M$ are constants. This approach provides an accurate description of the eventwise

TABLE II. Model parameters for central Au+Au collisions. Figure 9 shows the comparison of PM distributions using these parameters to measured STAR data.

| PM parameters, Au+Au collisions, $\sqrt{s_{NN}} = 200$ GeV | |
| --- | --- |
| $\langle p_T \rangle$ | 0.6 GeV/$c$ |
| $M$ | 600 |
| $R_{AA}, R = 0.2$ | 0.2 |
| $R_{AA}, R = 0.4$ | 0.2–0.5 |

distribution of transverse energy $E_T$ in high-energy nuclear collisions [71–73].

The hard jet yield per Au+Au collision is

$$\frac{dN_{\text{jet}}^{AA}}{dp_{T,\text{jet}}} = \frac{d\sigma_{pp}^{\text{jet}}}{dp_{T,\text{jet}}} \langle T_{AA} \rangle R_{AA} C(p_{T,\text{jet}}), \qquad (7)$$

where $\frac{d\sigma_{pp}^{\text{jet}}}{dp_{T,\text{jet}}}$ is the inclusive charged-particle jet cross section within $|\eta_{\text{jet}}| < 1$ for $pp$ collisions at $\sqrt{s} = 200$ GeV, calculated by PYTHIA; $\langle T_{AA} \rangle$ has value 22.8 mb$^{-1}$ for central Au+Au collisions; $R_{AA}$ is the jet yield suppression due to quenching, with value chosen such that the hard tail of the reconstructed jet distributions matches the data at high $p_{T,\text{jet}}$; and $C(p_{T,\text{jet}})$ is a function that cuts the $\frac{dN_{\text{jet}}^{AA}}{dp_{T,\text{jet}}}$ distribution off smoothly for $p_{T,\text{jet}}^{\text{ch}} \lesssim 4$ GeV/$c$, in order not to double-count soft particle production.

Table II shows the PM parameters used to model central Au+Au collisions at $\sqrt{s_{NN}} = 200$ GeV. The values for $\langle p_T \rangle$ and $M$ are similar to those observed in STAR data [11,81]. $R_{AA}$ is constant for $R = 0.2$ and a linear function of $p_{T,\text{jet}}^{\text{reco,ch}}$ for $R = 0.4$, to provide model variation that spans inclusive hadron measurements at RHIC and the LHC and jet measurements at the LHC (see Fig. 16). For these parameters, the integral of Eq. (7) for $p_{T,\text{jet}} > 4$ GeV/$c$ is 0.126, which is the average rate of such hard jets per central Au+Au collision. For PM event generation, the number of hard jets in each event is Poisson-distributed about this average, with $p_{T,\text{jet}}$ distributed according to Eq. (7), and with uniform distribution over the full azimuth and $|\eta| < 1$. PYTHIA fragmentation is then run for either a light quark or a gluon jet, chosen in ratio 2:1, with transverse momentum equal to $p_{T,\text{jet}}$. The charged particles generated by this procedure are the "hadrons" of the PM, comprising the hard jet component of PM events.

Figure 9 shows (quasi-)inclusive jet $p_{T,\text{jet}}^{\text{reco,ch}}$ distributions for various values of $p_{T,\text{lead}}^{\text{min}}$, for PM-generated events and for the STAR measurements in central Au+Au collisions shown in Fig. 3. The good level of agreement of the PM-generated distributions with data is notable, in light of the very simple nature of the model. For $p_{T,\text{lead}}^{\text{min}} = 5$ GeV/$c$, the PM-generated distributions agree with data within 10%, except in the extreme tails, over three orders of magnitude variation in yield. For $p_{T,\text{lead}}^{\text{min}} = 0$, the level of agreement is poorer, though the yields in this case vary by six orders of magnitude over the range of comparison. While the agreement of the model with data could be improved further by introducing additional parameters, the focus of this analysis is on $p_{T,\text{lead}}^{\text{min}} = 5$ GeV/$c$,

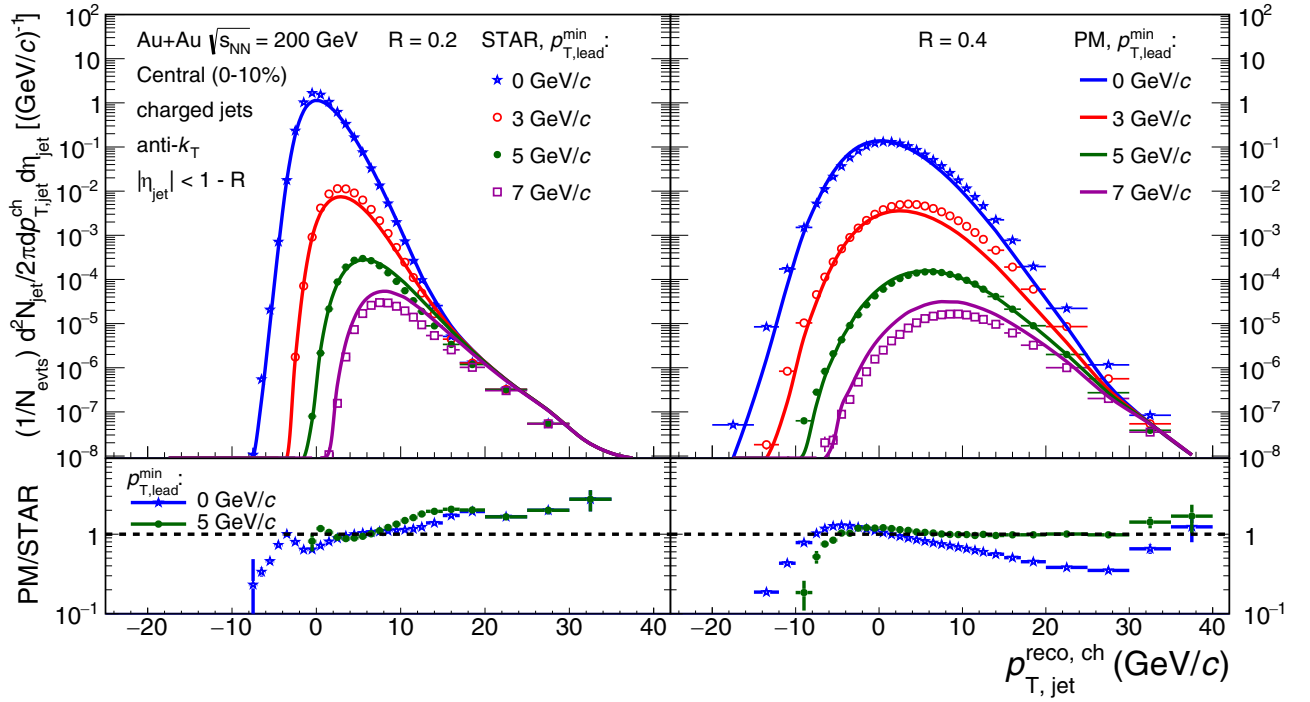FIG. 9. (Quasi-)inclusive jet $p_{T,\text{jet}}^{\text{reco,ch}}$ distributions for various values of $p_{T,\text{lead}}^{\text{min}}$ for $R = 0.2$ (left) and $R = 0.4$ (right), for PM-generated events and for the STAR measurements of central Au+Au collisions (data from Fig. 3). Lower panels show the ratio of the PM and data distributions, for $p_{T,\text{lead}}^{\text{min}} = 0$ and $p_{T,\text{lead}}^{\text{min}} = 5$ GeV/$c$.

where the agreement is already good, and we therefore choose not to do so.

Figure 9 shows that the background distribution in this analysis is driven predominantly by gross features of the collisions and measurement—acceptance, track multiplicity $M$, and $\langle p_T \rangle$—with dynamical correlations due to both soft and hard QCD processes playing a secondary or even negligible role. This picture, in which the background distribution is determined largely by statistical phase space, is consistent with that derived from the mixed event background analysis in Ref. [48].

We turn now to the closure test, to assess the validity of the correction procedure described above. Closure of this correction procedure for instrumental effects was shown in Ref. [48]. The focus of this closure test is therefore the large smearing of the jet spectrum due to fluctuations of uncorrelated background, which are well represented by the PM generator (Fig. 9).

The closure test utilizes 20M PM-generated events modeling central Au+Au collisions, which has similar statistical precision to the real dataset. The cut $p_{T,\text{lead}}^{\text{min}} = 5$ GeV/$c$ is imposed on all jet candidates. The full analysis to generate the $p_{T,\text{jet}}^{\text{ch}}$ distribution and to correct background fluctuations was then run, including generation of $\delta p_T$ distributions, unfolding, and the determination of systematic uncertainties.

Figure 10 shows the ratio of the corrected distributions from this procedure to the reconstructed hard jet distribution without background or detector effects ("Truth"), for $R = 0.2$ and $R = 0.4$. The ratio in the range $p_{T,\text{jet}}^{\text{ch}} > 15$ GeV/$c$ is

consistent with unity within uncertainties for both values of $R$. The ratio is, however, significantly above unity in the first bin at threshold, $p_{T,\text{lead}}^{\text{min}} = 5$ GeV/$c$. This feature is expected, since by construction the generated distribution has magnitude zero
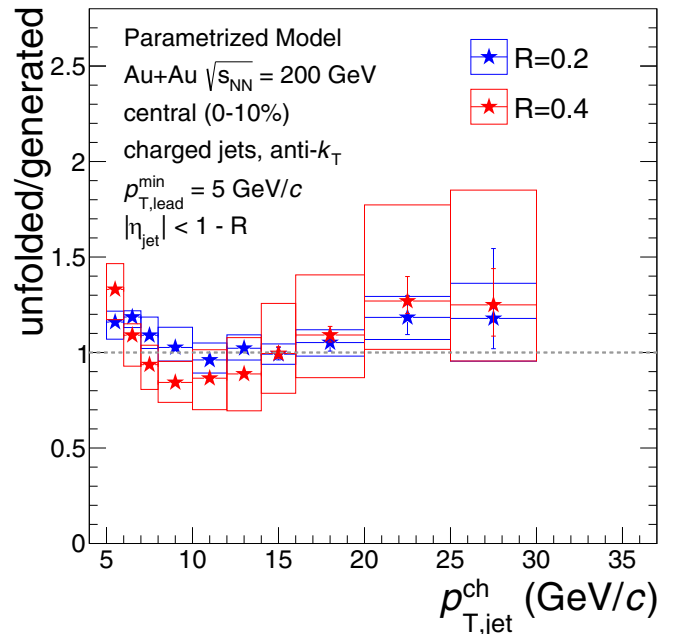


FIG. 10. Closure test for PM-generated events corresponding to central Au+Au collisions at $\sqrt{s_{NN}} = 200$ GeV.

for $p_{T,\text{jet}} < p_{T,\text{lead}}^{\min}$ and its magnitude is small and changing rapidly for $p_{T,\text{jet}}$ just above $p_{T,\text{lead}}^{\min}$, while the output of a regularized unfolding procedure cannot vary arbitrarily rapidly. In Sec. XI, the first bin at $p_{T,\text{jet}} = 5$ GeV/$c$ in the corrected distributions is therefore not shown. For larger values of $p_{T,\text{jet}}$, Fig. 10 validates the correction procedure for background fluctuations in this analysis.

## IX. REFERENCE SPECTRUM FROM *pp* COLLISIONS

The modification of inclusive jet production due to quenching is quantified by comparing measurements in central Au+Au collisions to those in smaller systems, specifically peripheral Au+Au and *pp* collisions. $R_{AA}$ is the ratio of inclusive yields in $A + A$ and *pp* collisions, with the latter scaled by $\langle T_{AA} \rangle$ to account for the effects of nuclear geometry. $R_{\text{CP}}$ is a similar ratio, in which the yield for peripheral Au+Au collisions is used as normalization.

The inclusive charged-particle jet spectrum in *pp* collisions at $\sqrt{s} = 200$ GeV is not currently available with statistical precision comparable to the inclusive charged-particle jet spectrum in central Au+Au collisions reported here. We therefore simulate the charged-particle jet distribution for *pp* collisions at $\sqrt{s} = 200$ GeV using PYTHIA Monte Carlo generator version 6.428 [83], with the Perugia 2012 tune (370) and CTEQ6L1 LO parton distribution functions [50]. However, a calculation of charged-pion yields using this PYTHIA tune overestimates the measured pion distribution by up to 30%. It was found that changing the PYTHIA parameter that controls the energy dependence of the low momentum cut-off for underlying event generation [PARP(90)] from its default value of 0.24 to 0.213 improves the agreement of the calculated inclusive pion yields with data, for both charged and neutral pions [51].

Figure 11 shows the comparison of PYTHIA-generated distributions using this tune with modified PARP(90) to inclusive pion measurements [55,82]; agreement of model and data is seen to be within 10% for $p_T > 3$ GeV/$c$. This configuration of PYTHIA is also in good agreement with measurements of inclusive jet yields, hadron distributions within jets, electromagnetic jet energy fraction, and dijet properties measured in *pp* collisions at $\sqrt{s} = 510$ GeV [51], and the underlying event measured in *pp* collisions at $\sqrt{s} = 200$ GeV [84]. These comparisons validate this PYTHIA-based calculation with modified tune for calculating inclusive jet $R_{AA}$ in the Au+Au analysis presented here.

The systematic uncertainty of the inclusive jet cross section generated by PYTHIA was estimated using several alternative PYTHIA tunes [83]: tune pairs 371 and 372 with $\alpha_s(\frac{1}{2}p_\perp)$ and $\alpha_s(2p_\perp)$ to vary the magnitude of initial- and final-state radiation; tune 374 with reduced color reconnection; tunes 376 and 377 with modified longitudinal and transverse fragmentation; and tune 383 with Innsbruck hadronization parameters. The tune pair 371 and 372, which bracket the distribution generated by the default PYTHIA tune and those of the other tunes, are used as the systematic uncertainty of the reference jet *pp* spectrum, corresponding to 22% for $R = 0.2$; 20% for $R = 0.3$; and 18% for $R = 0.4$, with negligible dependence on $p_{T,\text{jet}}$.
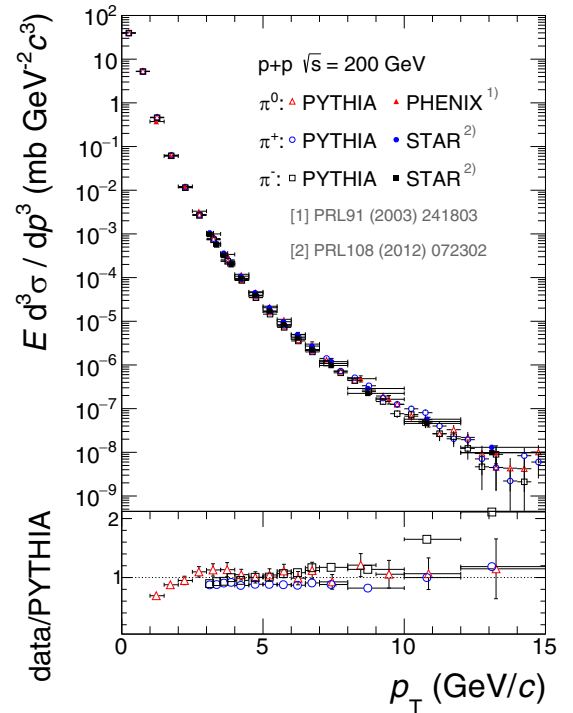


FIG. 11. Upper panel: Inclusive pion cross section in *pp* collisions at $\sqrt{s} = 200$ GeV from measurements [4,55,82] and from a PYTHIA simulation (see text for details). Lower panel: ratio of data and PYTHIA.

## X. THEORETICAL CALCULATIONS OF JET QUENCHING

We compare our results to several theoretical calculations incorporating jet quenching, which are labeled as follows:

  (i) NLO [85]: a next-to-leading-order (NLO) pQCD calculation that accounts for initial-state nuclear modification (EMC effect, initial-state energy loss) [86,87], with collisional partonic energy loss in the QGP calculated using a weak-coupling approach. This calculation provides a good description of the inclusive jet cross section for $R = 0.4$ in *pp* collisions at $\sqrt{s} = 200$ GeV [4] and predicts that inclusive jet $R_{AA}$ for $R = 0.2$ in Au+Au collisions at $\sqrt{s_{NN}} = 200$ GeV should be similar to $R_{AA}$ for neutral pions [19].

  (ii) SCET [88,89]: soft-collinear effective theory extended to describe jet propagation in matter (SCET$_G$) [90–92]; initial-state effects include dynamical nuclear shadowing, Cronin effect, and initial-state partonic energy loss. This approach describes well the measurement of charged-hadron $R_{AA}$ in Pb+Pb collisions at $\sqrt{s_{NN}} = 2.76$ TeV [22,24,93,94], though a similar level of agreement can be achieved with different parameter choices for initial state energy loss and Cronin effect, which are anticorrelated with $R_{AA}$ in the model. From the two SCET implementations available we use the one with slightly larger Cronin effect and smaller energy loss (SCET1). The error band for this model reflects two values of coupling constant *g* between the jet and the medium; the lower

edge of the band corresponds to $g = 2.2$, while the upper edge corresponds to $g = 2.0$.

(iii) Hybrid model [95]: combines several processes governing the evolution and interaction of jet showers in the medium. The production and evolution of the jet shower uses a weakly coupled approach based on PYTHIA, while the interaction of shower partons with the QGP uses a strongly coupled holographic approach based on $N = 4$ supersymmetric Yang-Mills theory. The model includes $p_T$-broadening of the shower in the QGP and back-reaction of the medium due to passage of the jet. The value of $\kappa_{\text{sc}}$, the free parameter in the model, was fixed by using LHC hadron and jet data as described in Ref. [96]. We note that calculations based on this global fit to LHC data disagree with measurements of high-$p_T$ hadron suppression at RHIC at the $3\sigma$ level, suggesting stronger jet-medium interaction at RHIC.

(iv) LBT model [97,98]: The Linear Boltzmann Transport model utilizes pQCD for elastic and inelastic scattering between jet shower and thermal medium partons. Dynamic evolution of the QGP is calculated using the 3+1D "CLVisc" hydrodynamic model [99], with initial conditions fluctuating event by event. The recoil of thermal partons is accounted for, enabling the calculation of medium response. LBT model calculations agree well with measurements of inclusive jet yield suppression in Pb+Pb collisions at the LHC [98].

(v) LIDO model [100,101]: The LIDO model is based on a modified formulation of semiclassical Boltzmann transport using pQCD cross sections with running coupling and an approximate treatment of in-medium multiple-scattering coherence (Landau-Pomeranchuk-Migdal or LPM effect). Medium excitation is accounted for using a linearized approximation to the hydrodynamic equations. LIDO model calculations reproduce inclusive jet and hadron suppression measurements in Pb+Pb collisions at the LHC. The LIDO calculations presented here [101] are shown as a band, corresponding to variation of the temperature-dependent coupling constant scale parameter between $1.5\pi T$ and $2\pi T$.

## XI. RESULTS

Figure 12 shows fully corrected quasi-inclusive charged jet distributions in central and peripheral Au+Au collisions at $\sqrt{s_{NN}} = 200$ GeV, for $R = 0.2$, 0.3, and 0.4, and for $p_{T,\text{lead}}^{\min} = 5$ and 7 GeV/$c$. The entire dataset is used for each distribution, which are therefore not statistically independent.

The requirement $p_{T,\text{lead}} > p_{T,\text{lead}}^{\min}$ imposes a bias on the reported jet population. This bias must be quantified in order to compare these data to other jet measurements and to theoretical calculations. The magnitude of the bias is expected to increase monotonically with increasing value of $p_{T,\text{lead}}^{\min}$, and we utilize that expectation to determine the range in $p_{T,\text{jet}}^{\text{ch}}$ in which the corrected distributions do not depend significantly on the value chosen for $p_{T,\text{lead}}^{\min}$.

We first explore the effect of the bias in $pp$ collisions at $\sqrt{s} = 200$ GeV, using PYTHIA simulations. Figure 13 shows the ratios of quasi-inclusive charged jet cross sections with $R = 0.2$ and 0.4 from this simulation for $p_{T,\text{lead}}^{\min} = 5$ GeV/$c$ relative to the unbiased distribution (labeled "5/0"), and $p_{T,\text{lead}}^{\min} = 7$ GeV/$c$ relative to $p_{T,\text{lead}}^{\min} = 5$ GeV/$c$ (labeled "7/5"). The ratio rises more rapidly above threshold for $R = 0.2$ than for $R = 0.4$, and more rapidly for 5/0 than 7/5. The bias due to $p_{T,\text{lead}}^{\min} = 5$ GeV/$c$ is less than 10% (i.e., the ratio 5/0 is larger than 0.9) for $p_{T,\text{jet}}^{\text{ch}} > 13$ GeV/$c$ for $R = 0.2$ and $p_{T,\text{jet}}^{\text{ch}} > 17$ GeV/$c$ for $R = 0.4$. The relative bias due to $p_{T,\text{lead}}^{\min} = 7$ GeV/$c$ relative to $p_{T,\text{lead}}^{\min} = 5$ GeV/$c$ is less than 10% (i.e., the ratio 7/5 is larger than 0.9) for $p_{T,\text{jet}}^{\text{ch}} > 19$ GeV/$c$ for $R = 0.2$ and $p_{T,\text{jet}}^{\text{ch}} > 24$ GeV/$c$ for $R = 0.4$. It is evident that measurement of the 7/5 ratio provides a conservative estimate of the range over which the bias due to choosing the value $p_{T,\text{lead}}^{\min} = 5$ GeV/$c$ is small.

Figure 14 shows the ratios of distributions from Fig. 12 for $p_{T,\text{lead}}^{\min} = 7$ GeV/$c$ and $p_{T,\text{lead}}^{\min} = 5$ GeV/$c$ for $R = 0.2$, 0.3, and 0.4 in peripheral and central Au+Au collisions. The systematic uncertainty of the ratio accounts for the correlated systematic uncertainties of numerator and denominator. For uncorrected distributions such a ratio must have value unity or below since the numerator is drawn from a subset of the data used in the denominator; however, the figure shows the ratio of corrected distributions, and such a constraint has not been imposed.

Figure 14 also shows the corresponding 7/5 ratios for $pp$ collisions simulated by PYTHIA (Fig. 13). The ratios for $pp$ collisions rise more slowly as a function of $p_{T,\text{jet}}^{\text{ch}}$ than those for peripheral Au+Au collisions and central Au+Au collisions, indicating differences in the distribution of high-$p_T$ jet fragments.

As discussed above for $pp$ collisions, the 7/5 ratio provides a conservative estimate of the region in which the bias due to the choice of value $p_{T,\text{lead}}^{\min} = 5$ GeV/$c$ is small. The ratios in Fig. 14 are consistent with or larger than 0.9 in the range $p_{T,\text{jet}}^{\text{ch}} > 15$ GeV/$c$ for jets with $R = 0.2$ and $p_{T,\text{jet}}^{\text{ch}} > 17$ GeV/$c$ for jets with $R = 0.3$ and 0.4. In the following figures we indicate these ranges by the label "∼unbiased."

Jet quenching may induce energy transport to angles larger than $R$ with respect to the jet axis, effectively suppressing the jet yield at a given value of $p_{T,\text{jet}}^{\text{ch}}$. In the next sections we discuss measurements of jet yield modification in central Au+Au collisions, using both the $R_{\text{CP}}$ and $R_{AA}$ observables.

### A. Yield suppression: $R_{\text{CP}}$

Figure 15 shows the distribution of $R_{\text{CP}}$ from this measurement, for $R = 0.2$, 0.3, and 0.4. Given the close similarity of the 7/5 ratio for central and peripheral Au+Au collisions shown in Fig. 14, we show $R_{\text{CP}}$ over the full measured range of $p_{T,\text{jet}}^{\text{ch}}$, without specification of an "Unbiased" region. The systematic uncertainty of $R_{\text{CP}}$ takes into account the correlated uncertainties of numerator and denominator. The uncertainty in the ratio due to $\langle T_{AA} \rangle$ is independent of $p_{T,\text{jet}}^{\text{ch}}$ and is
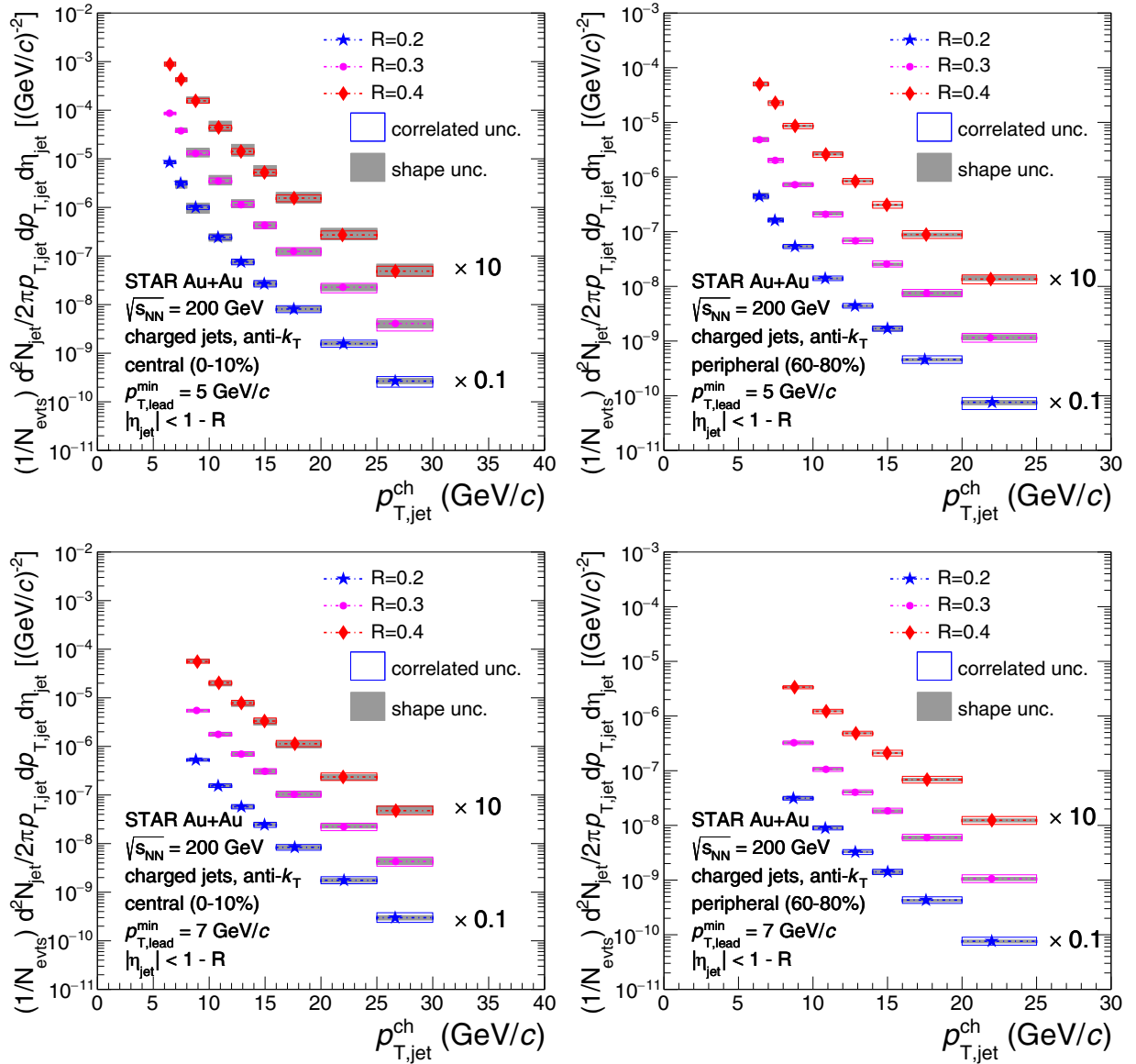
FIG. 12. Corrected quasi-inclusive charged-particle jet distributions in Au+Au collisions at $\sqrt{s_{NN}} = 200$ GeV for $R = 0.2$, 0.3, and 0.4. Left: Peripheral; right: central Au+Au collisions. Upper: $p_{T,\text{lead}}^{\text{min}} = 5$ GeV/$c$; lower: $p_{T,\text{lead}}^{\text{min}} = 7$ GeV/$c$. Correlated and shape systematic uncertainties are shown separately. The value of $p_{T,\text{jet}}^{\text{ch}}$ is shifted horizontally within each bin to account for the spectrum shape.

dominated by the uncertainty in $\langle T_{AA} \rangle$ for peripheral collisions. We observe that $R_{\text{CP}} \approx 0.4$ for all $R$, with at most a weak dependence on $p_{T,\text{jet}}^{\text{ch}}$.

Figure 16 compares $R_{\text{CP}}$ from Fig. 15 to that for charged jets with $R = 0.2$ and 0.3 measured in Pb+Pb collisions at $\sqrt{s_{NN}} = 2.76$ TeV [34], and to $R_{\text{CP}}$ for charged hadrons measured in Au+Au collisions at $\sqrt{s_{NN}} = 200$ GeV [15] and Pb+Pb collisions at $\sqrt{s_{NN}} = 2.76$ TeV [94]. Note that for this measurement, central and peripheral collisions correspond to the 0–10% and 60–80% percentile intervals of the Au+Au inelastic cross section, respectively, while for the LHC jet measurements in the figure the corresponding intervals are 0–10% and 50–80%; and for the charged hadron measurements at both RHIC and the LHC the centrality intervals are 0–5% and 60–80%.

The values of charged-hadron $R_{\text{CP}}$ at RHIC and the LHC agree within uncertainties over their common range in $p_T$. The magnitude of charged-particle jet $R_{\text{CP}}$ is likewise consistent within uncertainties at RHIC and LHC, though their $p_{T,\text{jet}}^{\text{ch}}$ intervals do not overlap. (Note that the bias due to $p_{T,\text{lead}}^{\text{min}} = 5$ GeV/$c$ is small for $p_{T,\text{jet}}^{\text{ch}} > 15$ GeV/$c$; see Fig. 14.) The apparent lack of dependence of charged-particle jet $R_{\text{CP}}$ on $p_{T,\text{jet}}^{\text{ch}}$ is in contrast to the significant $p_T$ dependence of charged-hadron $R_{\text{CP}}$.

The inclusive charged-hadron distribution at high-$p_T$ arises predominantly from the leading hadron of the corresponding jet. The correlation between hadron $p_T$ and its parent jet $p_{T,\text{jet}}^{\text{ch}}$ has a distribution that reflects the fragmentation process and which may generate different $p_T$ dependence of $R_{\text{CP}}$ for hadrons and jets. The comparison of hadron and jet suppres-
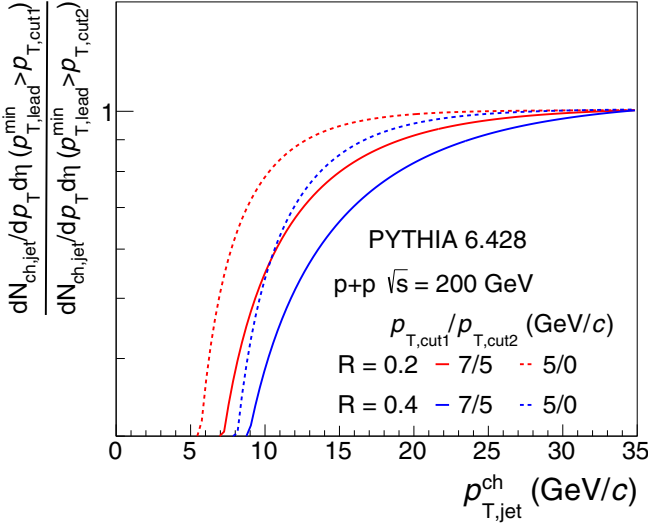
FIG. 13. Ratio of quasi-inclusive charged-particle jet cross sections simulated by PYTHIA for $pp$ collisions at $\sqrt{s} = 200$ GeV, $\eta_{\text{jet}} = 0$, for $R = 0.2$ (red) and 0.4 (blue), for $p_{T,\text{lead}}^{\min} = 5$ GeV/$c$ relative to the unbiased distribution ("5/0," dashed) and $p_{T,\text{lead}}^{\min} = 7$ GeV/$c$ relative to $p_{T,\text{lead}}^{\min} = 5$ GeV/$c$ ("7/5," solid).

sion in Fig. 16 thus provides new constraints on theoretical descriptions of jet quenching.

The suppression of $R_{\text{CP}}$ as a function of $p_{T,\text{jet}}^{\text{ch}}$ can be expressed equivalently as a $p_T$ shift of the spectrum in central, relative to peripheral, Au+Au collisions. This representation enables direct comparison of different suppression measurements since it removes the effect of the spectrum shape. The shift can be interpreted as the population-averaged energy transport out of the jet cone due to jet quenching [39,48]. Table III shows the $p_T$ shift values corresponding to $R_{\text{CP}}$ in Fig. 15 in the range $15 < p_{T,\text{jet}}^{\text{ch}} < 25$ GeV/$c$, chosen to minimize the effect of the bias due to the $p_{T,\text{lead}}^{\min}$ cut. The uncertainty in the value of the $p_T$ shift takes into account the correlated uncertainties of the central and peripheral Au+Au distributions.

Table III compares the $p_T$ shift measured in this analysis to that for semi-inclusive recoil jet yield suppression measured using hadron+jet correlations in Au+Au collisions at $\sqrt{s_{NN}} = 200$ GeV [48]. Note that the in-medium path-length distribution of jets contributing to the two measurements may differ [48]. While the central values of the $p_T$ shift for the inclusive jet distributions are consistently smaller than those for recoil jets, no significant difference in $p_T$ shift is observed within the uncertainties.

## B. Yield suppression: $R_{AA}^{\text{Pythia}}$

This section presents measurements of $R_{AA}^{\text{Pythia}}$, in which the reference is the inclusive charged-particle jet distribution
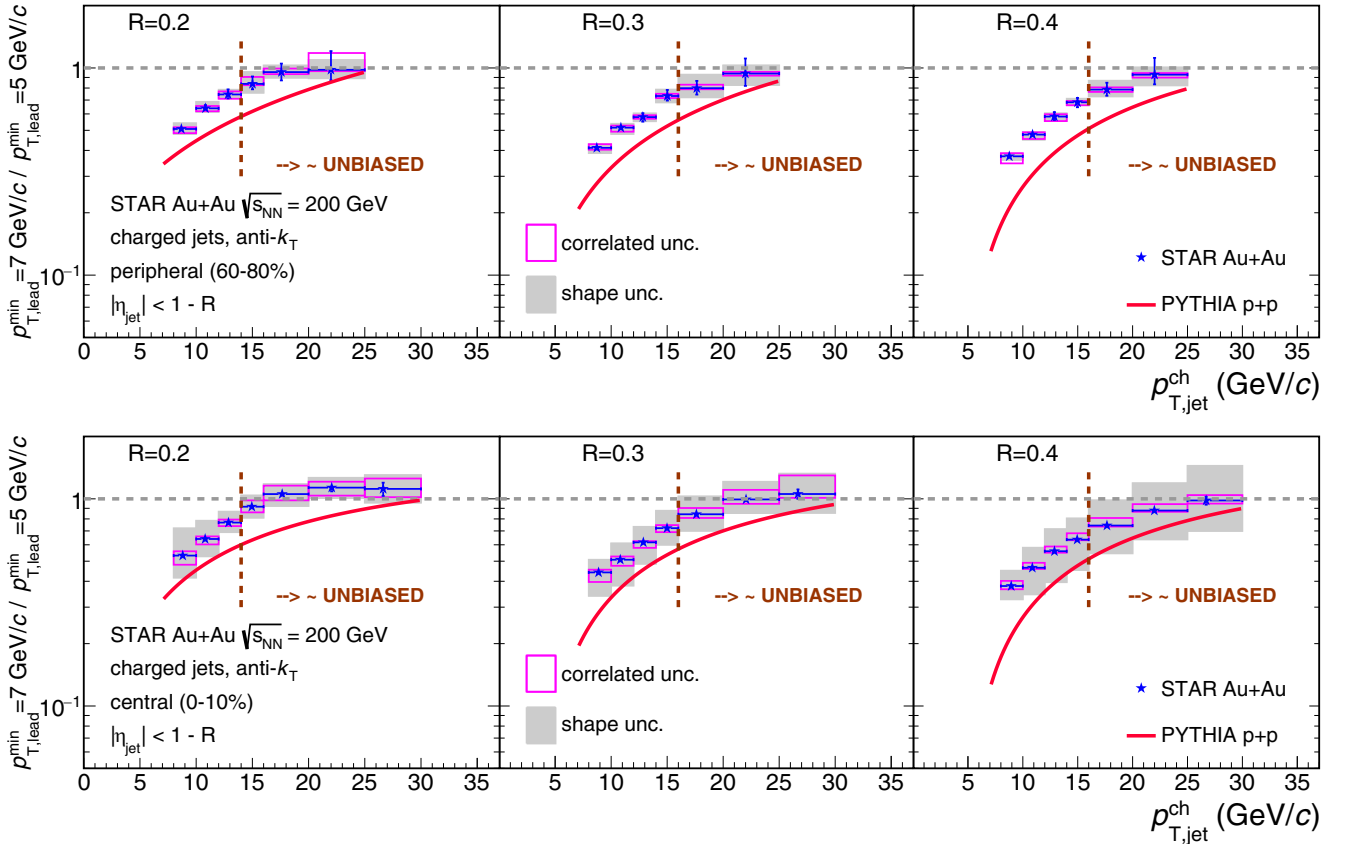


FIG. 14. Ratio of distributions from Fig. 12 for $p_{T,\text{lead}}^{\min} = 7$ GeV/$c$ and 5 GeV/$c$, for $R = 0.2$, 0.3, and 0.4 in peripheral (upper) and central (lower) Au+Au collisions. The red lines show the corresponding ratios from a PYTHIA simulation of $pp$ collisions (Fig. 13).
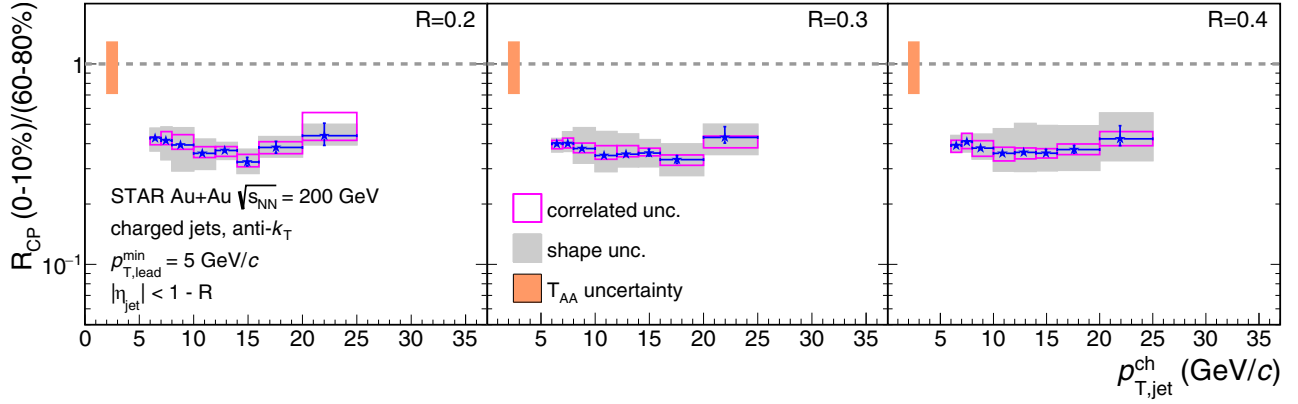
FIG. 15. $R_{CP}$ [(0–10%)/(60–80%)] for Au+Au collisions at $\sqrt{s_{NN}} = 200$ GeV, for $R = 0.2$, 0.3 and 0.4. See text for details.

for *pp* collisions at $\sqrt{s} = 200$ GeV calculated by PYTHIA, which was validated by comparing to other STAR hadron and jet measurements (Sec. IX). No $p_{T,\text{lead}}^{\min}$ cut is imposed on this reference jet population.

Figure 17 shows $R_{AA}^{\text{Pythia}}$ for quasi-inclusive jets in central Au+Au collisions at $\sqrt{s_{NN}} = 200$ GeV, for $R = 0.2$, 0.3 and 0.4. The region where the bias due to the $p_{T,\text{lead}}^{\min}$ cut is small for the central Au+Au collisions is indicated by the vertical dashed line.

Figure 18 compares $R_{AA}^{\text{Pythia}}$ from Fig. 17 to charged-hadron and $\pi^0$ $R_{AA}$ measured in Au+Au collisions at $\sqrt{s_{NN}} = 200$ GeV. The values of $\pi^0$ and jet $R_{AA}$ agree within uncertainties in this region.

Figure 19 compares measured charged-particle jet $R_{AA}$ to the theoretical calculations presented in Sec. X. The Hybrid, LBT, and LIDO calculations are carried out for charged jets, while the SCET and NLO pQCD calculations are for fully reconstructed jets. The $p_{T,\text{jet}}$ dependence of full jet $R_{AA}$ is weak, however, so that comparison of these calculations with the charged-particle jet measurement is meaningful. The LBT

and LIDO calculations also include a cut on the leading constituent for the Au+Au spectrum, corresponding to $p_{T,\text{lead}}^{\min} = 5$ GeV/$c$ applied in the data analysis. All calculations are consistent within uncertainties with the measured inclusive jet $R_{AA}$ in the unbiased region. The largest differences between models is seen for $R = 0.4$; future measurements of inclusive jet $R_{AA}$ with improved systematic precision may be able to discriminate between these models.

### C. Medium-induced jet broadening

The dependence of the inclusive jet yield on resolution parameter $R$ is sensitive to the jet energy profile transverse to its axis. Ratios of inclusive cross sections are of particular interest for measuring the transverse jet energy profile and its modification due to jet quenching since there is significant cancellation of systematic uncertainties in the ratio, both experimentally [6,103] and theoretically [95,104,105].

The ratio of inclusive jet cross sections for small $R$ ($R = 0.2$) and large $R$ ($R = 0.4$ or 0.5) is found to be less than
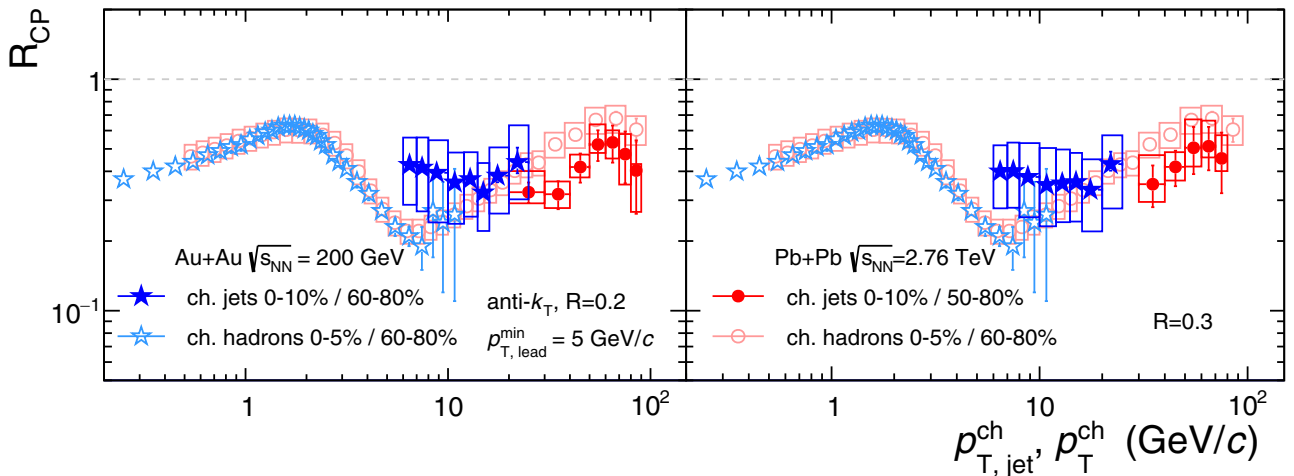


FIG. 16. $R_{CP}$ distributions from Fig. 15 compared to that measured in Pb+Pb collisions at $\sqrt{s_{NN}} = 2.76$ TeV [34], for $R = 0.2$ (left) and $R = 0.3$ (right). Also shown are $R_{CP}$ for inclusive charged hadrons in Au+Au collisions at $\sqrt{s_{NN}} = 200$ GeV [15] and in Pb+Pb collisions at $\sqrt{s_{NN}} = 2.76$ TeV [94]. Data from RHIC are in blue; data from the LHC are in red. The charged hadrons $R_{CP}$ distributions are the same in the two panels. The different choices of centrality class are discussed in the text.

TABLE III. $p_T$-shift between jet yield distributions in peripheral and central collisions normalized by the average number of binary collisions for quasi-inclusive jets (left) and semi-inclusive recoil jets (right).

| | Au+Au collisions, $\sqrt{s_{NN}} = 200$ GeV | |
|---|---|---|
| | $p_T$-shift peripheral$\rightarrow$central (GeV/$c$) | |
| $R$ | Quasi-inclusive jet (this analysis) $15 < p_{T,jet}^{ch} < 25$ GeV/$c$ | $h$+jet [48] $10 < p_{T,jet}^{ch} < 20$ GeV/$c$ |
| 0.2 | $-3.2 \pm 0.3_{stat} \pm 0.6_{sys}$ | $-4.4 \pm 0.2_{stat} \pm 1.2_{sys}$ |
| 0.3 | $-3.3 \pm 0.3_{stat} \pm 0.6_{sys}$ | $-5.0 \pm 0.5_{stat} \pm 1.2_{sys}$ |
| 0.4 | $-3.3 \pm 0.3_{stat} \pm 0.7_{sys}$ | $-5.1 \pm 0.5_{stat} \pm 1.2_{sys}$ |

unity in $pp$ collisions at $\sqrt{s} = 2.76$ and 7 TeV [6,103,106], consistent with pQCD calculations at NLO and next-to-next-to-leading-order (NNLO) [104,105]. A value of this ratio less than unity is expected qualitatively, since jets subtend finite area and larger-$R$ jet reconstruction collects more energy. However, the specific value of the ratio reflects the transverse jet energy profile: The areal energy density in a jet is on average largest near the jet axis, decreasing with increasing distance from the axis. The ratio of semi-inclusive recoil jet yields for different $R$ is likewise measured to be less than unity

in $pp$ collisions at $\sqrt{s} = 7$ TeV [39], with the ratio described better by PYTHIA than a pQCD calculation at NLO [39,107].

In nucleus-nucleus collisions, broadening of the transverse jet energy profile due to quenching has been explored by measuring the ratio of charged-particle jet inclusive cross sections with different $R$ in Pb+Pb collisions at $\sqrt{s_{NN}} = 2.76$ TeV [34], and the ratio of semi-inclusive recoil jet yields with different $R$ in Pb+Pb collisions at $\sqrt{s_{NN}} = 2.76$ TeV [39] and in Au+Au collisions at $\sqrt{s_{NN}} = 200$ GeV [48]. In both measurements, no significant medium-induced broadening is observed. Note that this observable is different from the jet shape observable employed in Refs. [108,109], with different experimental and theoretical uncertainties.

Figure 20 shows the ratio of distributions from Fig. 12 for $R = 0.2$ and 0.4, for central and peripheral Au+Au collisions. The measured ratio is less than unity for both centralities, as observed in $pp$ collisions [6,39,103,106]. The panels also show calculations for $pp$ collisions at $\sqrt{s} = 200$ GeV from PYTHIA and HERWIG, which agree within uncertainties with the ratios measured in Au+Au collisions. This indicates that there is no significant modification of the transverse jet profile due to quenching in central Au+Au collisions at $\sqrt{s_{NN}} = 200$ GeV, consistent with related measurements at RHIC and LHC [39,48,106].

This observation is in contrast to measurements of dijet asymmetry $A_J$ at RHIC [47], which find that energy lost due
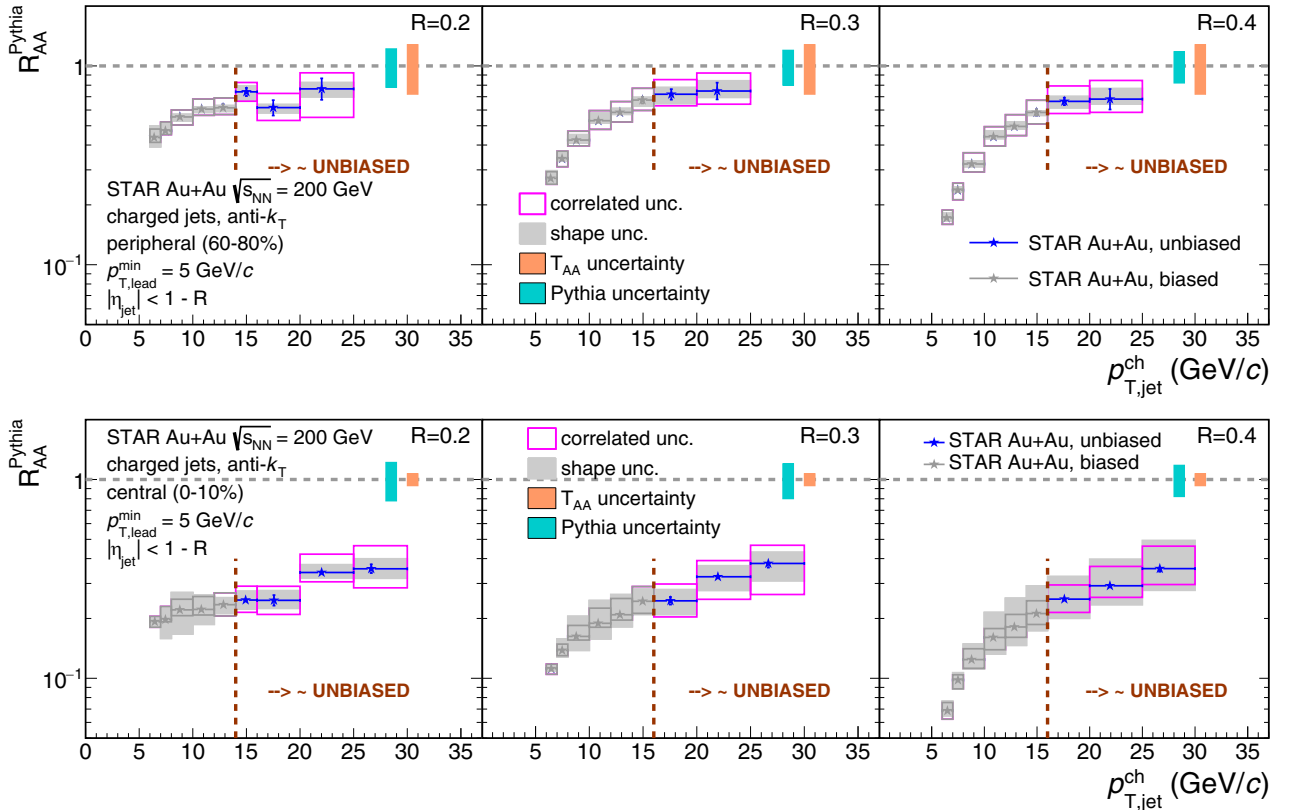


FIG. 17. $R_{AA}^{Pythia}$ for quasi-inclusive charged jets in peripheral (upper) and central (lower) Au+Au collisions at $\sqrt{s_{NN}} = 200$ GeV, for $R = 0.2$, 0.3, and 0.4. The reference spectrum for $pp$ collisions at $\sqrt{s} = 200$ GeV is generated by PYTHIA; see text for details. The region where the bias due to the $p_{T,lead}^{min}$ cut is small is indicated by the vertical dashed line.
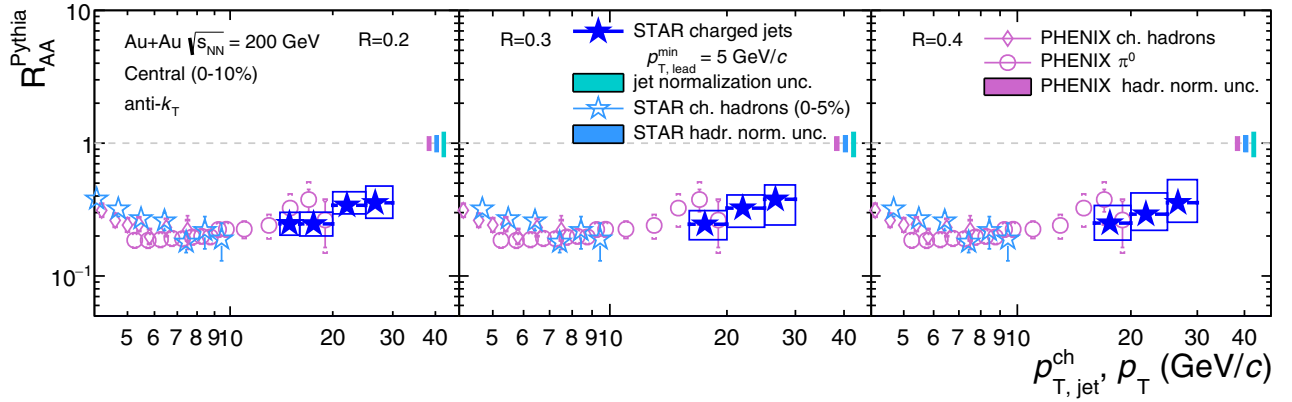
FIG. 18. Comparison of $R_{AA}^{\mathrm{Pythia}}$ from Fig. 17 (stars) to charged hadron [15,102] and $\pi^0$[19] $R_{AA}$ at $\sqrt{s_{NN}} = 200$ GeV. Only points from the region where the bias in the data due to the $p_{T,\mathrm{lead}}^{\min}$ cut is small are shown.
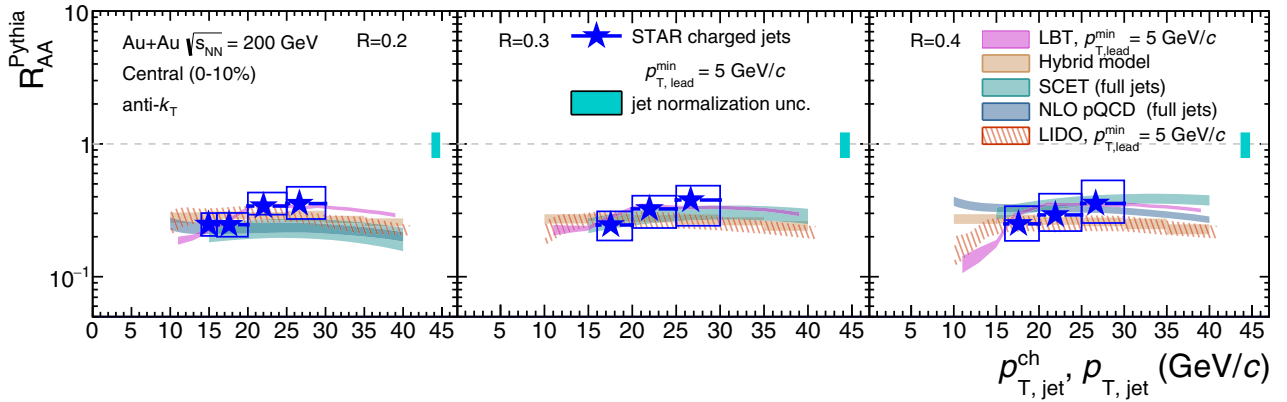


FIG. 19. Comparison of $R_{AA}^{\mathrm{Pythia}}$ from Fig. 17 (stars) to the theoretical calculations described in Sect. X. Only data in the unbiased region are shown. The Hybrid, LBT, and LIDO calculations are for charged-particle jets, while NLO and SCET are for fully reconstructed jets. The LBT and LIDO calculations account for the effect of $p_{T,\mathrm{lead}}^{\min} = 5$ GeV/$c$ in the Au+Au spectrum.
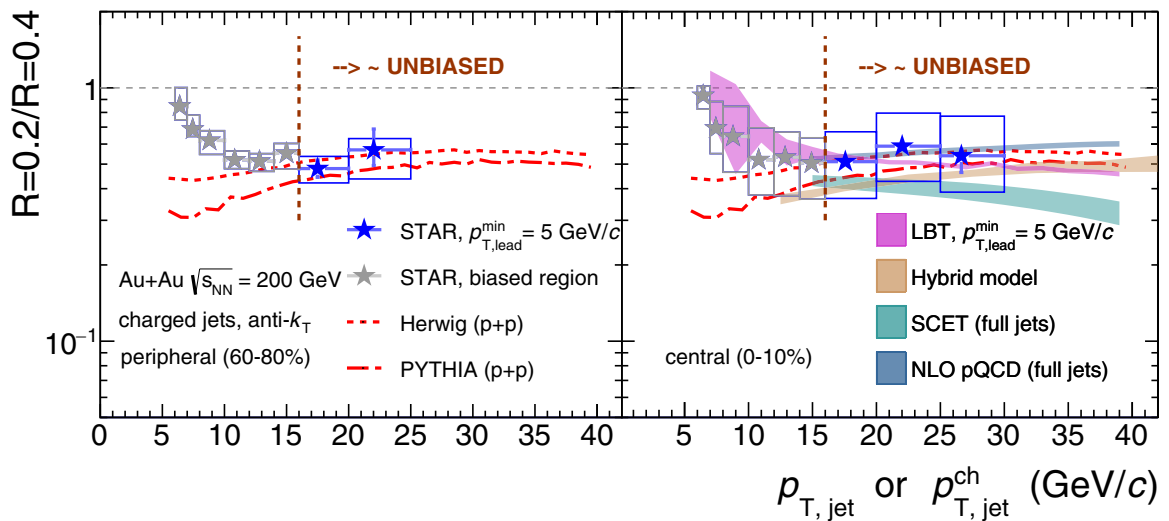


FIG. 20. Ratio of quasi-inclusive yields for charged jets with $R = 0.2$ and $R = 0.4$, for peripheral (left) and central (right) Au+Au collisions at $\sqrt{s_{NN}} = 200$ GeV and $p_{T,\mathrm{lead}}^{\min} = 5$ GeV/$c$. Calculations are shown for charged jets in $pp$ collisions at $\sqrt{s} = 200$ GeV simulated by PYTHIA [83] and HERWIG [110]; both panels show the same distributions from these calculations. Also shown are predictions for reconstructed jets in Au+Au collisions from the theoretical calculations described in Sect. X. The region where the bias due to the $p_{T,\mathrm{lead}}^{\min}$ cut is small is indicated by the vertical dashed line.

to quenching for jets with $R = 0.2$ is largely recovered for jets with $R = 0.4$, indicating a significant medium-induced modification of the transverse profile for the jet population selected in that analysis. However, that population differs significantly from the jet population used in the analysis reported here. Assessment of the two analyses and interpretation of their observed differences in terms of transverse jet profile modification requires the modeling of both measurements in a common theoretical framework (e.g., Ref. [111]).

Figure 20 (right panel) also shows theoretical calculations based on the Hybrid, LBT, NLO, and SCET models presented in Sec. X. These four models predict significantly different values for this ratio, though all calculations agree with the measurement within uncertainties. Future measurements of this observable, with improved systematic precision and at larger $R$, may discriminate between the models.

## XII. SUMMARY

We have reported the first measurement of inclusive charged-particle jet production in central and peripheral Au+Au collisions at $\sqrt{s_{NN}} = 200$ GeV, over the range $5 < p_{T,\text{jet}}^{\text{ch}} < 30$ GeV/$c$. The large uncorrelated background is suppressed by the requirement that the leading hadron in the jet satisfies $p_{T,\text{lead}} > p_{T,\text{lead}}^{\min}$, where $p_{T,\text{lead}}^{\min} = 5$ GeV/$c$. The bias imposed by this requirement is quantified by comparing distributions for $p_{T,\text{lead}}^{\min} = 5$ and 7 GeV/$c$, and the region of the measurement where the bias is small is identified.

A PM is developed, incorporating uncorrelated soft particle emission and a PYTHIA-generated jet distribution, motivated by the excellent description by such an approach of event-by-event transverse energy fluctuations in $A+A$ collisions over a wide range in $\sqrt{s_{NN}}$. The PM describes the uncorrected jet distributions in this analysis well, indicating that the background underlying jet measurements in central Au+Au collisions at RHIC is to a large extent statistically distributed, with dynamical correlations playing a much lesser role. This picture is also supported by an earlier mixed event analysis of semi-inclusive hadron-jet distributions at RHIC.

Comparison of the charged-particle jet yield in central and peripheral Au+Au collisions reveals a suppression for central Au+Au collisions, with magnitude of the suppression similar to that in central Pb+Pb collisions at the LHC. No significant $p_{T,\text{jet}}^{\text{ch}}$ dependence of inclusive jet suppression is observed, in contrast to the marked $p_T$ dependence of inclusive hadron suppression in central $A+A$ collisions at both RHIC and the LHC.

Jet yield suppression at fixed $p_{T,\text{jet}}^{\text{ch}}$ can be expressed equivalently as a shift in the yield distribution as a function of $p_{T,\text{jet}}^{\text{ch}}$, where the magnitude of the shift corresponds to medium-induced energy transport out of the jet cone. The $p_{T,\text{jet}}^{\text{ch}}$ shift for the inclusive jet population with $R = 0.4$ is $-3.3 \pm 0.3_{\text{stat}} \pm 0.7_{\text{sys}}$ GeV/$c$, consistent with that measured for semi-inclusive recoil jets. We note that in-medium path-length distributions for these two measurements may differ.

The charged-particle jet yield in central Au+Au collisions is also compared to that for $pp$ collisions generated by PYTHIA, which was validated using a STAR measurement of fully reconstructed jets in $pp$ collisions and inclusive single-particle spectra. The magnitude of suppression of inclusive $\pi^0$ and jet production from this comparison are consistent within uncertainties.

Comparison is also made to several theoretical calculations of jet quenching (NLO pQCD, SCET, Hybrid model, LIDO), which are consistent with the measurement within uncertainties. Greater precision is needed to discriminate the models.

Finally, medium-induced broadening of the jet transverse energy distribution is explored by measuring the ratio of inclusive yields for $R = 0.2$ and 0.4. No significant medium-induced modification is observed in central Au+Au collisions, consistent with similar measurements at the LHC. In comparison to jet quenching calculations, NLO predicts a larger ratio than that observed, but SCET and the Hybrid model are consistent with the measurement. The absence of medium-induced broadening in this inclusive jet analysis is in contrast to the broadening observed in dijet asymmetry measurements at RHIC. Interpretation of this difference requires modeling to carefully assess underlying biases in each of the two analyses.

The results presented here provide new constraints on theoretical models of jet quenching, and new insights into the nature of the large backgrounds to jet measurements in heavy-ion collisions.

[1] W. Busza, K. Rajagopal, and W. van der Schee, Annu. Rev. Nucl. Part. Sci. **68**, 339 (2018).
[2] U. Heinz and R. Snellings, Annu. Rev. Nucl. Part. Sci. **63**, 123 (2013).
[3] K. M. Burke *et al.*, Phys. Rev. C **90**, 014909 (2014).
[4] B. I. Abelev *et al.* (STAR), Phys. Rev. Lett. **97**, 252001 (2006).
[5] L. Adamczyk *et al.* (STAR), Phys. Rev. D **95**, 071103 (2017).
[6] B. Abelev *et al.* (ALICE), Phys. Lett. B **722**, 262 (2013).
[7] G. Aad *et al.* (ATLAS), J. High Energy Phys. 02 (2015) 153; 09 (2015) 141.
[8] V. Khachatryan *et al.* (CMS), J. High Energy Phys. 03 (2017) 156.
[9] A. Majumder and M. Van Leeuwen, Prog. Part. Nucl. Phys. **66**, 41 (2011).
[10] S. Cao and X.-N. Wang, (2020)arXiv:2002.04028 [hep-ph].
[11] J. Adams *et al.* (STAR), Nucl. Phys. A **757**, 102 (2005).
[12] X.-N. Wang and M. Gyulassy, Phys. Rev. Lett. **68**, 1480 (1992).
[13] C. Adler *et al.* (STAR), Phys. Rev. Lett. **89**, 202301 (2002).
[14] C. Adler *et al.* (STAR), Phys. Rev. Lett. **90**, 082302 (2003).
[15] J. Adams *et al.* (STAR), Phys. Rev. Lett. **91**, 172302 (2003).
[16] J. Adams *et al.* (STAR), Phys. Rev. Lett. **97**, 162301 (2006).
[17] L. Adamczyk *et al.* (STAR), Phys. Rev. Lett. **112**, 122301 (2014).
[18] K. Adcox *et al.* (PHENIX), Phys. Rev. Lett. **88**, 022301 (2002).
[19] A. Adare *et al.* (PHENIX), Phys. Rev. C **87**, 034911 (2013).
[20] A. Adare *et al.* (PHENIX), Phys. Rev. Lett. **104**, 252301 (2010).
[21] K. Aamodt *et al.* (ALICE), Phys. Rev. Lett. **108**, 092301 (2012).
[22] B. Abelev *et al.* (ALICE), Phys. Lett. B **720**, 52 (2013).
[23] J. Adam *et al.* (ALICE), Phys. Lett. B **763**, 238 (2016).
[24] S. Chatrchyan *et al.* (CMS), Eur. Phys. J. C **72**, 1945 (2012).
[25] S. Chatrchyan *et al.* (CMS), Eur. Phys. J. C **72**, 2012 (2012).
[26] R. Baier, Nucl. Phys. A **715**, 209 (2003).
[27] A. Drees, H. Feng, and J. Jia, Phys. Rev. C **71**, 034909 (2005).
[28] A. Dainese, C. Loizides, and G. Paic, Eur. Phys. J. C **38**, 461 (2005).
[29] K. Eskola, H. Honkanen, C. Salgado, and U. Wiedemann, Nucl. Phys. A **747**, 511 (2005).
[30] T. Renk, Phys. Rev. C **74**, 024903 (2006).
[31] C. Loizides, Eur. Phys. J. C **49**, 339 (2007).
[32] H. Zhang, J. Owens, E. Wang, and X.-N. Wang, Phys. Rev. Lett. **98**, 212301 (2007).
[33] T. Renk, Phys. Rev. C **86**, 061901 (2012).
[34] B. Abelev *et al.* (ALICE), J. High Energy Phys. 03 (2014) 013.
[35] J. Adam *et al.* (ALICE), Phys. Lett. B **746**, 1 (2015).
[36] S. Acharya *et al.* (ALICE), Phys. Rev. C **101**, 034911 (2020).
[37] G. Aad *et al.* (ATLAS), Phys. Rev. Lett. **114**, 072302 (2015).
[38] V. Khachatryan *et al.* (CMS), Phys. Rev. C **96**, 015202 (2017).
[39] J. Adam *et al.* (ALICE), J. High Energy Phys. 09 (2015) 170.
[40] G. Aad *et al.* (ATLAS), Phys. Rev. Lett. **105**, 252303 (2010).
[41] S. Chatrchyan *et al.* (CMS), Phys. Lett. B **712**, 176 (2012).
[42] S. Chatrchyan *et al.* (CMS), Phys. Lett. B **718**, 773 (2013).
[43] A. M. Sirunyan *et al.* (CMS), Phys. Rev. Lett. **121**, 242301 (2018).
[44] S. Acharya *et al.* (ALICE), Phys. Lett. B **776**, 249 (2018).
[45] S. Acharya *et al.* (ALICE), Phys. Lett. B **802**, 135227 (2020).
[46] A. M. Sirunyan *et al.* (CMS), Phys. Rev. Lett. **120**, 142302 (2018).
[47] L. Adamczyk *et al.* (STAR), Phys. Rev. Lett. **119**, 062301 (2017).
[48] L. Adamczyk *et al.* (STAR), Phys. Rev. C **96**, 024905 (2017).
[49] M. Cacciari, G. P. Salam, and G. Soyez, J. High Energy Phys. 04 (2008) 063.
[50] P. Z. Skands, Phys. Rev. D **82**, 074018 (2010).
[51] J. Adam *et al.* (STAR), Phys. Rev. D **100**, 052005 (2019).
[52] K. H. Ackermann *et al.* (STAR), Nucl. Instrum. Methods A **499**, 624 (2003).
[53] M. Anderson *et al.*, Nucl. Instrum. Methods A **499**, 659 (2003).
[54] J. Adams *et al.* (STAR), Phys. Lett. B **616**, 8 (2005).
[55] G. Agakishiev *et al.* (STAR), Phys. Rev. Lett. **108**, 072302 (2012).
[56] B. I. Abelev *et al.* (STAR), Phys. Rev. Lett. **97**, 152301 (2006).
[57] G. Agakishiev *et al.* (STAR), Phys. Rev. Lett. **108**, 072301 (2012).
[58] M. L. Miller, K. Reygers, S. J. Sanders, and P. Steinberg, Annu. Rev. Nucl. Part. Sci. **57**, 205 (2007).
[59] G. de Barros, B. Fenton-Olsen, P. Jacobs, and M. Ploskon, Nucl. Phys. A **910-911**, 314 (2013).
[60] M. Cacciari, G. P. Salam, and G. Soyez, Eur. Phys. J. C **72**, 1896 (2012).
[61] M. Cacciari, G. P. Salam, and G. Soyez, J. High Energy Phys. 04 (2008) 005.
[62] M. Cacciari and G. P. Salam, Phys. Lett. B **659**, 119 (2008).
[63] G. Cowan, Conf. Proc. C **0203181**, 248 (2002).
[64] A. Höcker and V. Kartvelishvili, Nucl. Instrum. Methods A **372**, 469 (1996).
[65] G. D'Agostini, (2010) arXiv:1010.0632 [physics.data-an].
[66] P. Jacobs (STAR), Nucl. Phys. A **855**, 299 (2011).
[67] A. Adare *et al.* (PHENIX), Phys. Rev. C **92**, 034913 (2015).
[68] G. D'Agostini, Nucl. Instrum. Methods A **362**, 487 (1995).
[69] A. Adare *et al.* (PHENIX), Phys. Rev. D **83**, 052004 (2011).
[70] L. Adamczyk *et al.* (STAR), Phys. Rev. C **92**, 024912 (2015).
[71] K. Adcox *et al.* (PHENIX), Phys. Rev. C **66**, 024901 (2002).
[72] J. Adams *et al.* (STAR), Phys. Rev. C **71**, 064906 (2005).
[73] L. Adamczyk *et al.* (STAR), Phys. Rev. C **87**, 064902 (2013).
[74] H. Appelshauser *et al.* (NA49), Phys. Lett. B **459**, 679 (1999).
[75] D. Adamova *et al.* (CERES), Nucl. Phys. A **727**, 97 (2003).
[76] S. S. Adler *et al.* (PHENIX), Phys. Rev. Lett. **93**, 092301 (2004).
[77] B. B. Abelev *et al.* (ALICE), Eur. Phys. J. C **74**, 3077 (2014).
[78] X.-N. Wang and M. Gyulassy, Phys. Rev. D **44**, 3501 (1991).
[79] I. Lokhtin, A. Belyaev, and A. Snigirev, Eur. Phys. J. C **71**, 1650 (2011).
[80] M. Tannenbaum, Phys. Lett. B **498**, 29 (2001).
[81] B. Abelev *et al.* (STAR), Phys. Rev. C **79**, 034909 (2009).
[82] S. S. Adler *et al.* (PHENIX), Phys. Rev. Lett. **91**, 241803 (2003).
[83] T. Sjöstrand, S. Mrenna, and P. Z. Skands, J. High Energy Phys. 05 (2006) 026.
[84] J. Adam *et al.* (STAR), Phys. Rev. D **101**, 052004 (2020).
[85] I. Vitev and B.-W. Zhang, Phys. Rev. Lett. **104**, 132001 (2010).
[86] I. Vitev and B.-W. Zhang, Phys. Lett. B **669**, 337 (2008).
[87] R. Sharma, I. Vitev, and B.-W. Zhang, Phys. Rev. C **80**, 054902 (2009).
[88] Y.-T. Chien and I. Vitev, J. High Energy Phys. 05 (2016) 023.

[89] Y.-T. Chien, A. Emerman, Z.-B. Kang, G. Ovanesyan, and I. Vitev, Phys. Rev. D **93**, 074030 (2016).

[90] A. Idilbi and A. Majumder, Phys. Rev. D **80**, 054022 (2009).

[91] F. D'Eramo, H. Liu, and K. Rajagopal, Phys. Rev. D **84**, 065015 (2011).

[92] G. Ovanesyan and I. Vitev, J. High Energy Phys. 06 (2011) 080.

[93] B. B. Abelev *et al.* (ALICE), Eur. Phys. J. C **74**, 3108 (2014).

[94] G. Aad *et al.* (ATLAS), J. High Energy Phys. 09 (2015) 050.

[95] J. Casalderrey-Solana, D. Gulhan, G. Milhano, D. Pablos, and K. Rajagopal, J. High Energy Phys. 03 (2017) 135.

[96] J. Casalderrey-Solana, Z. Hulcher, G. Milhano, D. Pablos, and K. Rajagopal, Phys. Rev. C **99**, 051901 (2019).

[97] Y. He, T. Luo, X.-N. Wang, and Y. Zhu, Phys. Rev. C **91**, 054908 (2015); **97**, 019902 (2018).

[98] Y. He, S. Cao, W. Chen, T. Luo, L.-G. Pang, and X.-N. Wang, Phys. Rev. C **99**, 054911 (2019).

[99] L.-G. Pang, Y. Hatta, X.-N. Wang, and B.-W. Xiao, Phys. Rev. D **91**, 074027 (2015).

[100] W. Ke, Y. Xu, and S. A. Bass, Phys. Rev. C **100**, 064911 (2019).

[101] W. Ke, X.-N. Wang, W. Fan, and S. Bass (2020), arXiv:2008.07622 [nucl-th].

[102] S. S. Adler *et al.* (PHENIX), Phys. Rev. C **69**, 034910 (2004).

[103] S. Chatrchyan *et al.* (CMS), Phys. Rev. D **90**, 072006 (2014).

[104] G. Soyez, Phys. Lett. B **698**, 59 (2011).

[105] M. Dasgupta, F. A. Dreyer, G. P. Salam, and G. Soyez, J. High Energy Phys. 06 (2016) 057.

[106] B. B. Abelev *et al.* (ALICE), Phys. Rev. D **91**, 112012 (2015).

[107] D. de Florian, Phys. Rev. D **79**, 114014 (2009).

[108] S. Chatrchyan *et al.* (CMS), Phys. Lett. B **730**, 243 (2014).

[109] V. Khachatryan *et al.* (CMS), J. High Energy Phys. 11 (2016) 055.

[110] M. Bahr *et al.*, Eur. Phys. J. C **58**, 639 (2008).

[111] K. Kauder (JETSCAPE), Nucl. Phys. A **982**, 615 (2019).